High-Temperature Materials

SCIEPublish

Article

Characterization and Thermal Study of Raw and Purified Pyrophyllites

Pedro J. Sánchez-Soto [1,†], Vanesa García-Garzón [2,†], Eduardo Garzón [2,*], Juan A. Sánchez-Garrido [3,*], Luis Pérez-Villarejo [4] and Sergio Martínez-Martínez [5]

[1] Institute of Materials Science of Seville (ICMS), Joint Center Spanish National Research Council (CSIC)-University of Seville, c/Americo Vespucio 49, 41092 Seville, Spain; pedroji@icmse.csic.es (P.J.S.-S.)

[2] Department of Engineering, University of Almería, La Cañada de San Urbano s/n, 04120 Almería, Spain; vanessagarciagarzon@gmail.com (V.G.-G.)

[3] Department of Agronomy, University of Almería, La Cañada de San Urbano s/n, 04120 Almería, Spain

[4] Department of Chemical, Environmental and Materials Engineering, Higher Polytechnic School of Linares, University of Jaén, 23700 Linares (Jaén), Spain; lperezvi@ujaen.es (L.P.-V.)

[5] Department of Mechanical and Mining Engineering, Higher Polytechnic School of Linares, University of Jaén, 23700 Linares (Jaén), Spain; smartine@ujaen.es (S.M.-M.)

* Corresponding author. E-mail: egarzon@ual.es (E.G.); jasanche@ual.es (J.A.S.-G.)

† These authors contributed equally to this work.

Received: 7 March 2026; Revised: 30 March 2026; Accepted: 22 April 2026; Available online: 8 May 2026

ABSTRACT: Pyrophyllite is a 2:1 layered silicate with interest in ceramics, refractories, and several other important applications. In this work, an investigation into the thermal behaviour of several natural and purified pyrophyllite samples, including a pyrophyllite clay, has been conducted. A previous characterization of these samples has been carried out by AA, XRD, thermal analysis by thermo-dilatometry and DTA-TG, surface area, and SEM-EDX. Thus, relevant chemical, mineralogical, thermal, and textural data of these samples have been obtained. As a second step of this investigation, the thermal behaviour of these pyrophyllite samples has been investigated by XRD and SEM after several thermal treatments at 800, 1100 and 1150 °C during 24 h. The formation of dehydroxylated pyrophyllite as a crystalline phase in the samples was established after 1050 °C by XRD, and its permanency above this temperature, with little changes in morphological features, as revealed by SEM. When thermal treatment was progressive at higher temperatures (1300 °C) the following was evidenced by XRD: (a) the formation and crystallization of mullite ($3Al_2O_3 \cdot 2SiO_2$), with a progressive destruction of dehydroxylated pyrophyllite, and (b) the formation of cristobalite (SiO_2). This later phase was formed by crystallization of the amorphous silica, detected as a hump by XRD, which is segregated in the solid-state reaction of formation of mullite. This treatment produces a new microstructure with elongated and needle-like crystals of mullite according to SEM observations. All these results have been found of interest for the preparation of ceramic materials, mullite-based ceramics, and refractories using these pyrophyllite samples.

Keywords: Pyrophyllite; Dehydroxylated pyrophyllite; Mullite; Cristobalite; Chemical analysis; Thermal treatment; Crystallization; Microstructure; Ceramics; Refractory materials

© 2026 The authors. This is an open access article under the Creative Commons Attribution 4.0 International License (https://creativecommons.org/licenses/by/4.0/).

1. Introduction

Pyrophyllite and talc are both 2:1 layered hydrous silicates, with structural differences from kaolinite, which is a 1:1 layered silicate [1–7]. The structure of pyrophyllite and talc is based on an octahedral sheet (O) with Al^{3+} (in pyrophyllite) or Mg^{2+} (in talc) between two opposite tegrahedral sheets (T) or T-O-T structure, with the ideal formulas $Al_2Si_4O_{10}(OH)_2$ [or $Al_2O_3 \cdot 4SiO_2 \cdot H_2O$] and $Mg_3Si_4O_{10}(OH)_2$ for pyrophyllite and talc, respectively [1–9]. Thus, in pyrophyllite, there are octahedrally coordinated Al^{3+} sheets between two sheets of SiO_4 tetrahedra. Figure 1 shows the structure of the 2:1 layered silicate pyrophyllite compared to the 1:1 layered silicate kaolinite $Al_2Si_2O_5(OH)_4$. The theoretical composition of pyrophyllite is 66.7 wt. % of SiO_2, 28.3 wt. % of Al_2O_3 and 5.0 wt. % of H_2O (structural water). The structural water in pyrophyllite and talc, both 2:1 layered silicates, is lost by thermal treatments at temperatures lower than 1000 °C but higher than in kaolinite [10].

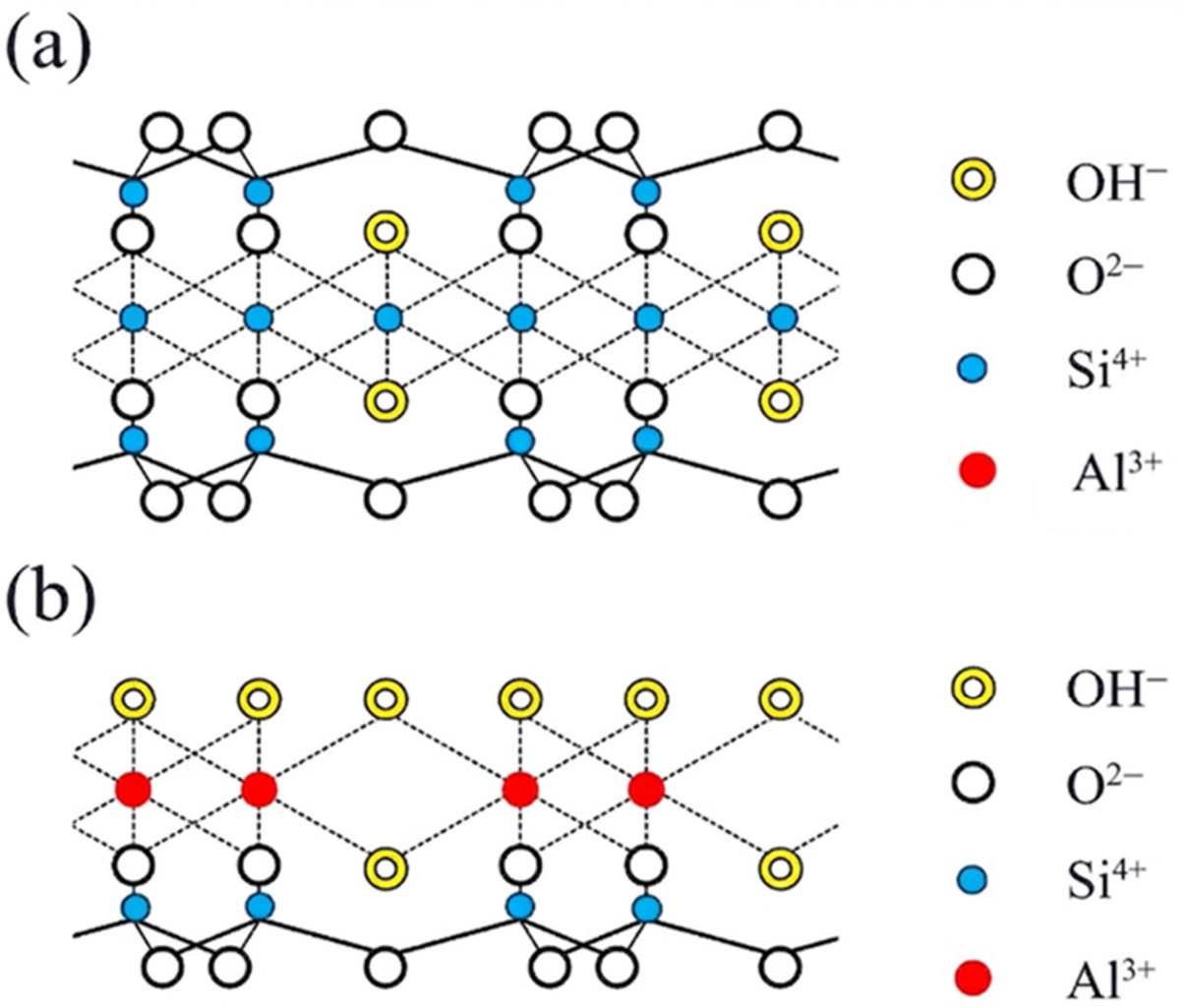

Figure 1. (**a**) Crystal structure of 2:1 layered silicate pyrophyllite and (**b**) 1:1 layered silicate kaolinite.

Pyrophyllite resembles talc according to its physical properties, for instance, in softness and structural features, similar to talc [3,5–7], showing complete exfoliation along *001* and good thermal, insulating, and electrical properties, although the main difference is the content of Al or Mg. Pyrophyllite and talc show different chemical properties and thermal resistance [3,7–10]. Furthermore, pyrophyllite appears in nature associated with kaolinite and kaolinitic clays, muscovite mica/illite or sericite, feldspars and other silicates,

besides quartz and iron and titanium oxides [2,6–9]. Besides this, several researchers have studied the formation of pyrophyllite solid solutions and the identification of pyrophyllite polytypes and mixed layers-[11–14].

Commercial deposits of pyrophyllite have been found mainly in Japan, the USA (North Carolina, California, and others), Australia, New Zealand (Coromandel), South Africa, China, Thailand, Korea, Saudi Arabia, India, Russia, Canada, Peru, and Brazil [15–38]. In Spain, pyrophyllite has been found associated with kaolinite and muscovite mica/illite or sericite [24–27,31–34].

In general, pyrophyllite and pyrophyllite clays have good and interesting technological properties. However, it should be noted that several studies focused on the effects of pyrophyllite powders on the cell [39], metabolic activity of some microorganisms [40], and pyrophyllite dust control [41]. Even more, the potential in biomedical applications, with studies in genotoxicity, has been investigated [42]. It is very interesting when pyrophyllite is used as a carrier for different types of medicaments. The pyrophyllite surface can be modified to be applied in composites with polymers, for instance styrene [43] and polyurethane [44], besides as a silica-alumina support of catalysts [45,46]. Adsorption properties of pyrophyllite have also been examined [44,47–50].

Pyrophyllite, with an average particle size of 4.80 μm, has been applied to prepare low-cost ceramic membranes for treating industrial and domestic wastewaters [51,52] and as a raw material for road surfacing aggregates with interesting properties [53]. The application of pyrophyllite as a solid pressure transmitting media for diamond synthesis at high pressures and temperatures has been recognized after several studies [54–58]. Thus, the mechanical properties under these conditions have been studied [58].

Several important applications of pyrophyllite are based on its thermal decomposition, yielding a material with a low expansion coefficient, low thermal and electrical conductivity, excellent reheating stability, and low reversible thermal expansion. Consequently, pyrophyllite has been applied as a ceramic raw material, for instance, in the preparation of stoneware bodies, china (porcelain) products, triaxial porcelains, ceramic tiles, insulating firebricks, foundry specialties, whiteware bodies, earthenware tiles, glass production, sealants, and refractory compositions [59–80]. For instance, Tauber and Pepplinkhouse replaced silica by pyrophyllite in vitreous china products [62,63]. Amritphale et al. [64] studied the energy-efficient process for making pyrophyllite-based ceramic tiles. It has been mentioned that pyrophyllite can be used as a raw material to reduce energy consumption [65]. Furthermore, the effect of pyrophyllite on the mullitization in the triaxial porcelain system has been studied by Mukhopadhyay et al. [66–68]. However, some of these raw materials, considered as “pyrophyllite”, in fact, are pyrophyllite mixed with muscovite/illite or sericite or a sericitic/muscovitic pyrophyllite mineral [24–27,32,67,68]. These raw materials, sometimes considered as sericitic clays with pyrophyllite or aluminium shales with pyrophyllite [32], are very interesting as precursors of mullite [69–71], for instance, to prepare high-porosity mullite-corundum ceramics with sericite induced textured structures [70].

An important application of pyrophyllite is its use as a raw material for high-temperature refractories [72–80]. As relevant examples, refractories based on unfired andalusite-pyrophyllite [73], with high-mullite content by a mixture of pyrophyllite-gibbsite [74], alumina substrates [75], refractory enamels [15], and refractory composites [80], have been prepared and studied. It is relevant to remark that refractory materials based on zircon ($ZrSiO_4$) and pyrophyllite [77–79] are of great interest for high-temperature uses. Zircon-based materials can be agglomerated using pyrophyllite, yielding materials inside the ZrO_2–Al_2O_3–SiO_2 ternary equilibrium phase diagram, with special application in contact zones with melt glasses [79]. Besides this, it has been proposed that pyrophyllite, like other aluminosilicates and clays, can be used to prepare silicon nitride and sialon-based ceramic materials by carbothermal reduction and reactive nitridation [81–85]. Sialon and Sialon matrix composites are high-temperature structural ceramic materials with excellent resistance to oxidation, corrosion, and mechanical properties [83–85].

Composites using carbon black and pyrophyllite clays have been prepared by Kanbara et al. [86]. These kinds of composites are chemically stable, porous, and electrically conductive with potential application as

electrodes in batteries and condensers. Other researchers have focused on the development of a modified pyrophyllite carbon paste electrode for the detection of highly toxic chemicals with endocrine-disrupting effects and pronounced carcinogenicity used in agricultural production as pesticides [87]. Cui et al. [88] reported the synthesis and characterization of a UV-resistant ZnO-pyrophyllite nanocomposite prepared by solid-state reaction method using a pyrophyllite raw material (Taining, Fujian Province, China). MacKenzie et al. [89] have prepared geopolymers using pyrophyllite (2:1 layered silicate), an innovation because a wide range of geopolymers has been prepared using kaolinite (1:1 layered silicate) thermally treated to produce metakaolinite [90].

Antimicrobial properties of pure and modified pyrophyllite with Ag have been studied by Jelić et al. [91]. Recently, novel clay/Ag system, such as the synthesis of pyrophyllite/$AgNO_3$ composites, has been prepared and studied by Mijaković et al. [92]. This kind of composites expands potential applications of Ag-doped pyrophyllite (pyrophyllite/$AgNO_3$ composites) as Ag-novel clays in important fields, such as electrochemistry, biomedicine, and environmental protection [91,92]. According to the above, the applications of this 2:1 layered silicate are being enlarged, and the economic value added could be further increased.

Several researchers, using various experimental techniques such as X-ray diffraction (XRD), Transmission Electron Microscopy, and Solid-State Nuclear Magnetic Resonance, have studied the thermal transformations of pyrophyllite [2,4,93–109]. At the beginning of these studies, the crystalline phase formed by dehydroxylation of pyrophyllite was named as "pyrophyllite anhydride" or "anhydrous pyrophyllite", having investigated the thermal behaviour of several pyrophyllite samples [2,4,93,94]. This phase is a crystalline phase, retaining a well-organized structure, after examination by XRD. It is in contrast with "metakaolinite", which is amorphous to X-rays, being produced by dehydroxylation of kaolinite (1:1 layered silicate) by thermal treatments at temperatures lower than 900 °C [90,106]. First of all, the crystalline phase named as "pyrophyllite anhidride" [2] was considered a dehydroxylated phase by Wardle and Brindley [4] and posterior researchers [95–109]. Molina-Montes et al. [107,108] have proposed the presence of different possible intermediates during the dehydroxylation of pyrophyllite. Pérez-Rodríguez et al. [109] studied in deep the dehydroxylation-rehydroxylation of pyrophyllite. The rehydroxylation process was found to be influenced by pyrophyllite particle size and to depend on the dehydroxylation temperature.

It should be noted that Wardle and Brindley [4] determined by XRD the crystal structure of pyrophyllite and its dehydroxylated phase and proposed a structural model. The model is based on a substitution of OH^- groups by O^{2-} in an intermediate position between adjacent Al^{3+}, with a distorted trigonal bipyramidal configuration with AlO_5 structural units and five-coordinated Al^{3+}. An experimental result reported by these scholars to support the proposed structural model was the data of average distance Al–O (determined by XRF) equal to 0.180 nm, which is intermediate between 0.170 and 0.174 nm for Al in tetrahedral coordination and 0.190–0.194 nm for Al in octahedral coordination. However, the value of 0.180 nm could be the result of a 1:1 mixture of Al in octahedral and tetrahedral coordination [4]. It should be noted that the X-ray diffractometric technique is used to study the long-range order, and, as a complementary technique, solid-state Magic-Angle Spinning (MAS) Nuclear Magnetic Resonance (NMR) spectroscopy is used to study the short-range order. Then, all the Al^{3+} in octahedral coordination in pyrophyllite would be pentahedrally coordinated in the dehydroxylated phase, as demonstrated several years after Wardle and Brindley [4]. In fact, it was proposed that dehydroxylation of pyrophyllite above 800 °C produced solid-state NMR spectra of 27-Al associated with a distorted trigonal bipyramidal configuration, being all Al^{3+} pentahedrally coordinated [95–97,99,100,103]. Thus, the dehydroxylation reaction concerning aluminum is according to the scheme:

$$Al^{VI}O_4(OH)_2 \rightarrow Al^{V}O_5 + H_2O \quad (1)$$

When pyrophyllite is subjected to thermal treatments at increasing temperatures, the dehydroxylated phase is decomposed at temperatures higher than 1200 °C, yielding mullite ($3Al_2O_3 \cdot 2SiO_2$) and cristobalite (SiO_2) as high-temperature phases [93–100]. The stoichiometric reactions are as follows:

$$Al_2Si_4O_{10}(OH)_2 \rightarrow Al_2Si_4O_{11} + H_2O \quad (2)$$

$$3Al_2Si_4O_{11} \rightarrow 3Al_2O_3 \cdot 2SiO_2 + 10SiO_2 \quad (3)$$

From these solid-state reactions, it is deduced that the relative proportion of mullite obtained from pyrophyllite thermal decomposition is lower than that obtained from kaolinite $Al_2Si_2O_5(OH)_4$ thermal decomposition [90,104,106].

In a pioneering study on the thermal transformation of pyrophyllite to mullite, it was reported by Heller [93] that this solid-state reaction is topotactic. This scholar suggested that Al^{3+} migrates into the mullite and liberates excess silica, which crystallizes as cristobalite with increasing temperatures. Many years later, after Heller's study [93], it was possible to investigate the mechanism of mullite and cristobalite formation from dehydroxylated pyrophyllite by the development of the MAS-NMR spectroscopy technique [95–97,99,100,103]. Thus, it was examined in deep the process of tetrahedral sheet breakdown by progressive thermal treatments and the subsequent Al and Si local rearrangement to originate mullite ($3Al_2O_3 \cdot 2SiO_2$) and cristobalite (SiO_2). According to the MAS-NMR results reported by Sánchez-Soto et al. [100,104], when tetrahedral sheet breakdown takes place in dehydroxylated pyrophyllite, there is a segregation of amorphous silica, according to reaction (2), which permits rearrangements of Al^{3+} and favours the formation of mullite as disordered nuclei. The pentahedral Al coordination present in dehydroxylated pyrophyllite progressively changes as the temperature, with the formation of these disordered mullite nuclei and detection, by NMR, of tetrahedral and octahedral Al coordination associated to this high-temperature phase [100,104]. The thermal transformation of pyrophyllite to mullite is interesting, where mullite, as an advanced material, is necessary for structural, electronic, thermal, and optical applications [110–114].

The aim of this paper is to investigate the thermal behaviour of several pyrophyllite samples, natural and purified, and the formation of high-temperature phases (mullite and cristobalite), performing a comparative study, with the purpose of an evaluation of possible applications. A characterization by several techniques of the original samples and after thermal treatments was performed in order to know the main features of all these pyrophyllite samples.

2. Materials and Methods

2.1. Starting Materials

A sample of pyrophyllite (Hillsboro, NC, USA) was used as starting material. The original sample was lightly ground and sieved under 100 µm. This sample was designed as PyH. A sample of pyrophyllite (Pambula, Australia) was used as received. This sample was ground by the supplier and sieved under 74 µm, being designed as PyA. A sample of pyrophyllite clay (Zalamea de la Serena, Badajoz, Spain), designed ZS (with 90% fraction < 63 µm), was also considered in the present study. This sample was purified by chemical acid treatment, using a method previously described [115–117]. The method is based in a selective acid dissolution using a finely ground sample treated with a mixture of aqueous HNO_3 (1+4), aqueous $HClO_4$ (1+4), and HF (concentrated 40% *w*/*w*) and evaporated to dryness. The cooled residue was treated with aqueous $HClO_4$ (1+4) and evaporated to dryness again. The residue was treated with diluted HCl, separated by centrifugation, washed several times with water (distilled), and finally dried (60 °C) using an oven. This pyrophyllite sample was designed as PyP.

2.2. Preparation of Thermally Treated Samples

A laboratory furnace model RT-1600 from the Company CHESA (Madrid, Spain), with SiC heating elements, was used for thermal treatments of pyrophyllite samples in air. Alumina crucibles were used as containers for the powdered solids. A heating rate of 60 °C/min was selected up to several temperatures (800, 1100, and 1150 °C) during 24 h, as maximum, and then slowly cooled inside the furnace to room temperature. Fresh samples were used each time for these thermal treatments. Thermally treated samples were ground in an agata mortar and stored in a dried atmosphere before examination.

2.3. Experimental Methods

Chemical analysis of the samples was performed by Atomic Absorption (AA) using a Perkin Elmer equipment, model 703 (Waltham, MA, USA). The samples were ground using an agata mortar and pestle before chemical dissolution following a previous protocol [115].

X-ray diffraction powder diagrams (XRD) were obtained using a diffractometer Kristalloflex Siemens Aktiengesellschaft, Model D-500 (Karlsruhe, Germany), with Ni-filtered CuK_α radiation, at 36 kV and 26 mA, and a scanning rate of 1° 2θ/min.

Specific surface areas were determined by adsorption of N_2 at liquid Nitrogen temperature (77.35 K), based on the point b method [118], using a Micromeritics automated system, model 2200A, after preparing degassed samples by thermal treatment at 150 °C/2 h under N_2 (99.99% purity) flow. Samples were weighed before treatments, and specific surface areas were calculated in m^2/g with an accuracy of 99%, a reproducibility of 99.5%, and an estimated error of ±4%.

Differential Thermal Analysis (DTA) and Thermogravimetric analysis (TG) were carried out simultaneously using a Thermal Analyzer Thermoflex Rigaku Company, Model PTC-10 A (Tokyo, Japan), with data processing system DPS-1, and Pt/Pt-Rh 13% thermocouple with a grafite furnace using Argon to avoid oxidation of this material at a heating rate of 12 °C/min in static air. Calcined alumina (1300 °C) was the reference material for DTA runs. Samples (~40 mg) were packed loosely into a platinum holder and weighed in the TG system.

Thermo-dilatometric analysis was performed using a thermoanalytical high-temperature dilatometer Adamel-Lhomargy, Model D-24 (Roissy-en-Brie, France), at a heating rate of 6 °C/min, and SiC heating elements. Samples were prepared as pellets using powders pressed at 10 MPa.

Scanning Electron Microscopy (SEM) was used to examine original and thermally treated samples. Samples were deposited as powders on sample holders. In the case of pressed samples, thermally treated, it was performed a previous chemical etching using an aqueous solution of 20 vol. % HF. Fresh fractured surfaces of thermally treated samples were etched for 5 min using the HF solution. After that, the etched samples were washed with distilled water and ultrasonically treated for 10 min, washed with water and etanol and dried at 40 °C using an oven for 24 h. The equipment was an ISI apparatus, model SS-40, fitted to a Kevex energy dispersive X-ray analyzer, model 8000. Samples were coated with a thin gold films using a Blazer sputtering device to make them conductive.

3. Results and Discussion

3.1. Chemical Analysis

The results of chemical analysis of all the pyrophyllite samples are compared with the theoretical values for pyrophyllite (Table 1). These results are in well agreement with previous results published in the literature [17–23,28,30–38,84,88]. Samples PyH, PyA, and PyP have SiO_2 percentages in the range 62–69.5 wt. % and sample ZS is an outsider with a value lower (51.78 wt. %) than the theoretical pyrophyllite (66.65 wt. %). In contrast, sample PyH shows 66.42 wt. % of SiO_2 a percentage closer to the theoretical (66.65 wt. %). However, sample PyA shows a SiO_2 percentage of 69.45 wt. %, the highest of all the samples.

This result does not exclude the additional presence of free SiO_2, associated to quartz and other silicates. The percentages of Al_2O_3 follow the same trend in samples PyH, PyA, and PyP, with the lower percentage in the case of sample PyA and a value closer to the theoretical (28.35 wt. %) in sample PyH.

Table 1. Chemical analysis of pyrophyllite samples.

Composition (wt. %)	PyH	PyA	PyP	ZS	Theoretical Pyrophyllite
SiO_2	66.42	69.45	62.70	51.78	66.65
Al_2O_3	27.31	24.24	26.89	34.69	28.35
Fe_2O_3	0.20	0.24	0.08	0.61	-
TiO_2	0.10	0.10	5.76	1.46	-
CaO	0.09	0.09	0.12	0.35	-
MgO	0.01	0.03	0.06	0.22	-
Na_2O	0.10	0.15	0.08	0.45	-
K_2O	0.24	0.45	0.00	1.86	-
L.O.I.	5.41	4.83	4.27	8.31	5.00
Total	99.88	99.58	99.96	99.73	100.00
$[SiO_2/Al_2O_3]$	4.13	4.87	3.96	2.53	4.00
Δ(sample-theoretical)	0.13	0.87	0.04	1.47	-

In the case of sample ZS, the percentage of Al_2O_3 is the highest (34.69 wt. %), being associated to the presence of mineral phases more rich in Al_2O_3, possibly other layered silicates such as kaolinite and/or muscovite mica/illite or sericite. The $[SiO_2/Al_2O_3]$ molar ratio values and the differences with theoretical pyrophyllite, minimum in the case of PyP and maximum in the case of PyA, suggest the presence in these samples of mineral phases different of pyrophyllite. Sample ZS is an outsider as considered above.

The $[SiO_2/Al_2O_3]$ molar ratio is closer to the theoretical value (difference is 0.04). In fact, the "loss on ignition" (LOI) is very close to the theoretical value (5.00 wt. %) in samples PyH and PyA, showing differences in the other samples. Sample ZS presumably contains other layer silicates, with structural OH groups, which are lost by thermal treatments and, hence, contribute to the observed value of LOI.

In sample PyP, the majority of impurity oxides is TiO_2, which is associated with the chemical procedure to obtain this purified pyrophyllite [115]. Pyrophyllite shows a high resistance to acid attack. Taking into account the structure of this layered silicate (Figure 1), the reasons of this behaviour must be the unstrained structure and the position of the oxygen atoms, just between the layers [116,117].

According to the results of Table 1, in general, the percentages of iron oxide are lower than 0.7 wt. % in all the pyrophyllite samples, with a maximum value (0.61 wt. %) in sample ZS. The percentages of TiO_2 are lower in samples PyH and PyA, relatively high in sample ZS, and maximum in sample PyP, as indicated above. The percentages of K_2O, except in sample PyP, suggest the presence of alkaline mineral phases, such as feldspars or muscovite mica/illite or sericite, in particular in samples PyA, with 0.45 wt. % of K_2O, and sample ZS, with 1.86 wt. % of this oxide.

According to Zaykov and Udachin [35], it is possible to classify the types of raw pyrophyllites in relation to other raw materials, taking into account the chemical composition demanded by the industry for several applications (thermally resistant, ceramics, *etc*.). It can be mentioned that high-grade pyrophyllite ores are scarce [28,30,37,38,65,68,119–126]. Besides this, impurities such as Fe_2O_3 and TiO_2 lower the quality of the refractories prepared using pyrophyllite [120]. Filler-grade pyrophyllite requires a content of these oxides lower than $Fe_2O_3 < 0.5\%$ and $TiO_2 < 1\%$ [121]. Other authors investigated samples considered as pyrophyllite or pyrophyllite ores, although after a deep study, they reported the association of sericite in these "pyrophyllite" samples [68], as found in sample ZS of the present study. It should be noted that illite

and sericite are naturally occurring clay grade micas. Sericite is a fine-grained, soft mica mineral that contains K_2O in its structure, and is very similar to muscovite and illite [69–71].

3.2. Mineralogical Analysis

Figures 2 and 3 show the XRD patterns of the samples. It can be identified that pyrophyllite is the main crystalline phase in all the samples except ZS, besides a minor relative proportion of other silicates, such as kaolinite and muscovite mica/illite or sericite, according to their characteristic *d*-spacings. In sample ZS, the mineral phases pyrophyllite, kaolinite, and muscovite mica/illite or sericite are identified. Quartz is not present, or it is at a very low relative proportion to be detected by XRD, except in sample PyA, as expected by the chemical analysis (Table 1). Rutile (TiO_2) is identified in sample PyP, being associated to the chemical treatment that finally concentrates this mineral phase in the purified pyrophyllite sample [115], as mentioned in the precedent subsection. In general, these X-ray results are in accordance with the chemical characterization of the samples.

On the other hand, the study of the pyrophyllite polytypes may be difficult in all these samples according to the previous research on this subject [4,9–14]. However, after examination in detail of the XRD patterns, it can be deduced that Triclinic pyrophyllite (1Tc) is predominant in sample PyP, and possibly there is a mixture of Triclinic (1Tc) and Monoclinic (2M) pyrophyllite in samples PyH and PyA.

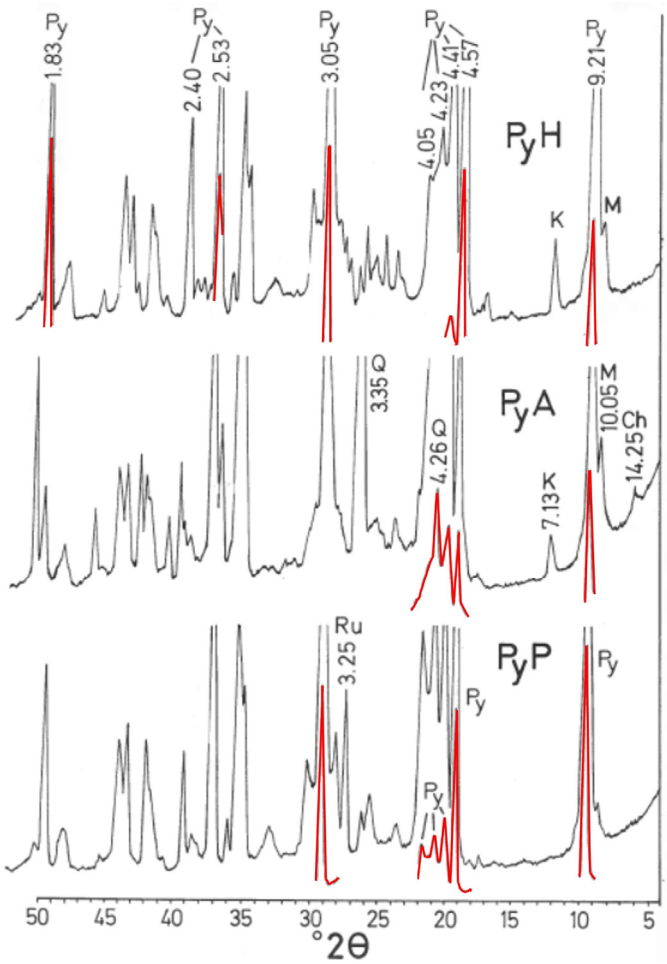

Figure 2. X-ray diffraction diagrams (XRD) of pyrophyllite samples PyH, PyA and PyP. The numbers are selected *d*-spacings of the mineral phases in Å (1 Å = 0.1 nm). Red colours of some peaks indicate the exact position of the X-ray peaks in these XRD obtained under enhanced experimental conditions, because it was possible in the X-ray equipment to diminish the conditions to record the intensity of the peaks. Note: Py = Pyrophyllite; K = Kaolinite; M = Muscovite/Illite; Q = Quartz; Ch = Chlorite; Ru = Rutile.

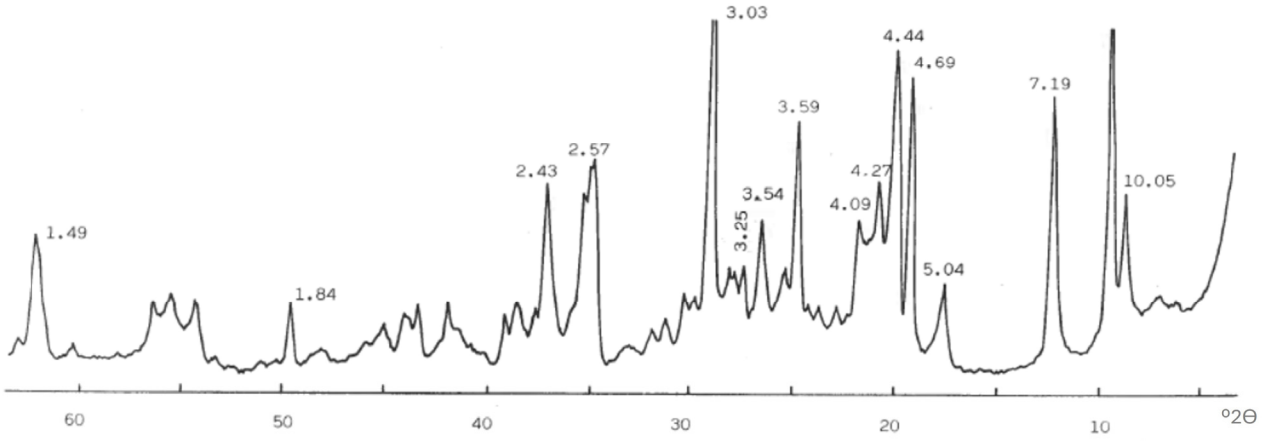

Figure 3. XRD of pyrophyllite clay sample ZS. The numbers are selected *d*-spacings of the mineral phases in Å (1 Å = 0.1 nm).

3.3. Specific Surface Areas

The results of the specific surface areas of all the samples are presented in Table 2. Sample PyH shows the minimum value of this parameter, followed by sample PyP. However, comparatively, samples PyA and ZS show higher values of specific surface areas, in particular sample ZS with the maximum value. Possibly, these results can be explained by a previous grinding in sample PyA, with pyrophyllite and quartz, which produces an increasing of specific surface area by reduction of the original particle sizes [14,122,123]. For instance, Gücek et al. [124] have reported a value of 7.03 m^2/g in a sample of pyrophyllite (lump-sized samples of pyrophyllite ore from Malatya (Turkey) subjected to crushing and grinding in a ball mil, followed by sedimentation to produce fines < 2 μm). Besides this, in sample ZS there is a mixture of minerals distinct of pyrophyllite, as detected by XRD (Figure 3), which could produce an increasing in specific surface area as compared with samples with higher relative proportions of pyrophyllite (Figure 2).

Table 2. Results of specific surface áareas (S) and average particle sizes (d) obtained from these data for the pyrophyllite samples.

	PyH	**PyA**	**PyP**	**ZS**
S (m^2/g)	0.63	5.20	1.17	12–44
d (μm)	3.41	0.41	1.83	0.17

Assuming spherical particles and taking into account the density (ρ) of pyrophyllite (2.8 g/cm^3) and the formula $d = 6/(\rho S)$, being *d* the average particle size (in μm), the values of *d* were calculated for all the samples, considered the "geometrical average particle size". They are included in Table 2. It can be seen that the sample with a lower average particle size (0.17 μm) is ZS. In this sample, it is clear that the presence of kaolinite and muscovite mica/illite or sericite, layered silicates with lower particle sizes as compared to pyrophyllite, is a factor of influence in this estimation. However, to calculate *d* in this sample, it was considered the density value of pyrophyllite, and sample ZS is a mixture, in fact, of several mineral phases as identified by XRD (Figure 3). The true density of this clay sample was determined, and an average value of 2.72 ± 0.2 g/cm^3 was obtained. Using this value and the value of specific surface area (Table 2) and the above formula, the calculated particle size is d = 0.17 μm, with limits 0.16 and 0.19 μm. On the other hand, the sample PyA shows an average particle size of 0.41 μm, being associated to a previous grinding treatment as indicated by the supplier. Finally, samples with pyrophyllite as the predominant phase (PyH and PyP) and without intensive grinding treatment show the higher values of the geometrical average particle size. These features can be evidenced by a SEM study, as described in the next subsection.

3.4. SEM-EDX of Original Samples

Figures 4 and 5 show selected SEM micrographs of all the samples. Figure 4a corresponds to the pyrophyllite sample PyH, with observation of large flat plates grouped as book-like formations. Analysis by EDX (Figure 4b) was consistent with the chemical composition of these plates, which was typical of pyrophyllite (see Table 1).

Figure 4c shows a selected micrograph corresponding to the pyrophyllite sample PyA, where pyrophyllite plates of several sizes can be observed. Some of them are fractured. There are particles, for instance at the right of the SEM micrograph (Figure 4c), with a different morphology, associated to quartz grains of different sizes present in this sample, as confirmed by chemical analysis by EDX (Figure 4d). It is in accordance with the previous identification of this mineral phase by XRD (Figure 2).

Figure 5a corresponds to a selected SEM micrograph of pyrophyllite sample PyP, where flat plates of several sizes can be observed. Some small elongated particles (size ~1 μm) present in this sample can be associated with rutile (TiO_2), as identified by XRD (Figure 2). According to the EDX analysis (Figure 5b), Ti is detected in these isolated particles in an Al–Si matrix, associated with pyrophyllite flat particles. Figure 5c shows a selected SEM micrograph corresponding to the sample ZS, the pyrophyllite clay, where a large plate of pyrophyllite can be observed besides of the presence of smaller plates, possibly of kaolinite or muscovite mica/illite or sericite, all these mineral phases identified by XRD (Figure 2). The EDX analysis (Figure 5c), with detection of potassium (K) in a silicon-aluminium matrix, confirmed the presence of muscovite mica.

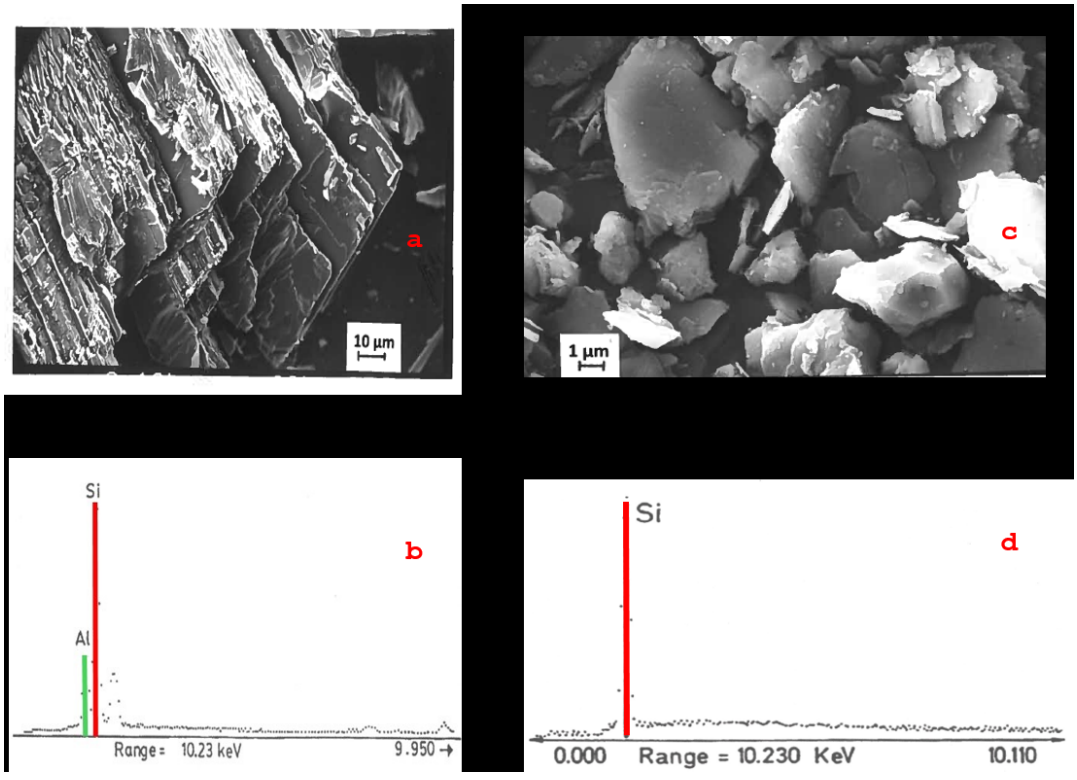

Figure 4. (**a**) Selected SEM micrographs of pyrophyllite sample PyH and (**b**) representative EDX analysis of a plate, (**c**) pyrophyllite sample PyA and (**d**) EDX analysis of a particle identified as quartz in this sample.

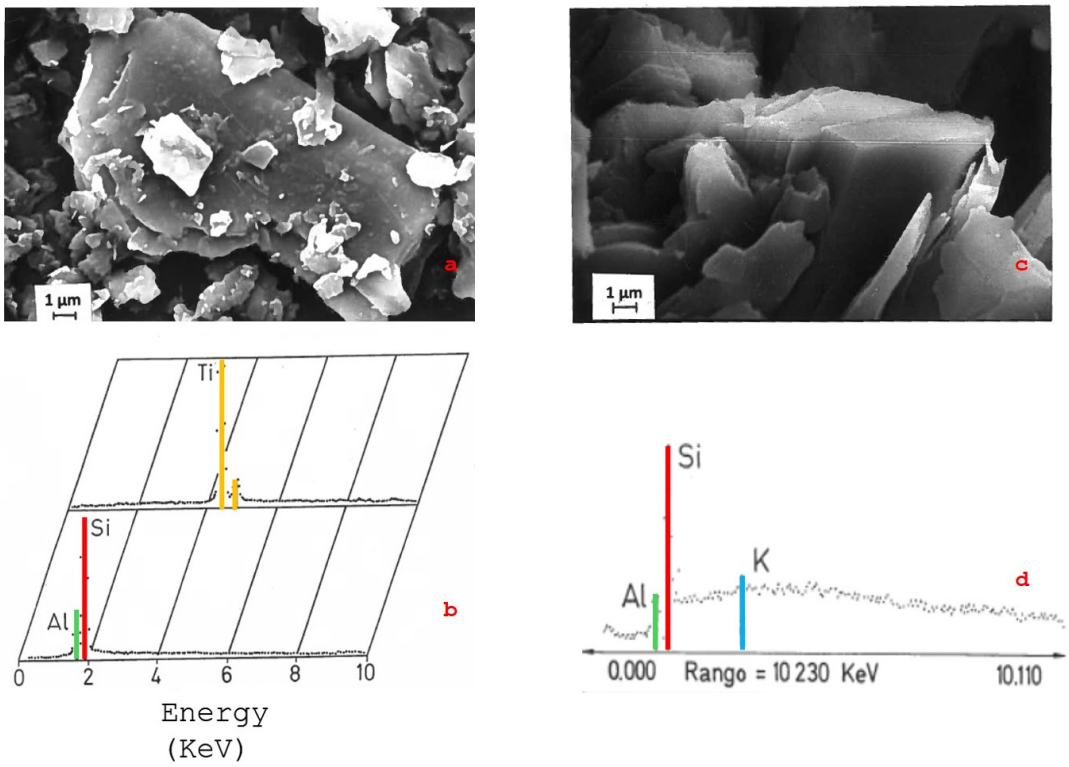

Figure 5. (**a**) Selected SEM micrographs of pyrophyllite sample PyP and (**b**) representative EDX analysis of a pyrophyllite plate and an elongated particle identified as rutile, (**c**) pyrophyllite clay sample ZS, and (**d**) EDX analysis of a plate which contains Al, Si, and K, associated to muscovite mica/illite or sericite.

It can be noted that a sample of pyrophyllite (Maharashtra, India), examined by SEM, showed "large flat crystals, with occasional book like stacked structure", along with some flaky-structured materials associated with micaceous minerals, because the sample is a pyrophyllite sericitic/muscovitic mineral [68]. Cui et al. [88] examined by SEM a sample of pyrophyllite raw material, obtained from Taining, Fujian Province, China. These authors observed a layered structure in this sample and an average grain size of 3.8 µm. Zhang et al. [125] studied a sample of pyrophyllite (Zhejiang province, south-eastern region of China), showing microstructural characteristics of lamella when this sample was examined by SEM. Ahmed et al. [126], studying a Saudi low-grade pyrophyllite ore (Pyrophyllite Mine in Yanbu, Saudi Arabia), reported a fine schistose texture, with pyrophyllite particles highly foliated and composed of fine particles and anhedral flakes. These flakes are arranged with sizes of ~2–4 µm in width and 0.1 µm in thickness. Rajić et al. [127] studied a pyrophyllite ore (Parsovići mine, Bosnia and Herzegovina), with the mineral composition of pyrophyllite, kaolinite, muscovite, calcite, and quartz. These authors observed by SEM particles showing a lamellar structure and a rough surface.

3.5. Differential Thermal Analysis (DTA) and Thermogravimetric Analysis (TG)

Figure 6 includes the DTA-TG diagrams of the samples containing the major proportion of pyrophyllite. The mass loss of the TG diagram associated to the dehydroxylation reaction of pyrophyllite starts from 500 °C. In sample PyP the mass loss starts from 600 °C. The dehydroxylation involves the reaction of 2 OH groups (adjacent to each other) coordinated to Al^{3+} in the structure and elimination of water. The total mass loss (~5 wt. %) is reached at 950–1000 °C in all the pyrophyllite samples. The calculated values of total mass loss for all the pyrophyllite samples are coincident with the results of "loss on ignition". These results are included in Table 1. They are near the theoretical value for an ideal pyrophyllite except in sample PyP, which contains more impurity oxides, mainly TiO_2, than PyH and PyA.

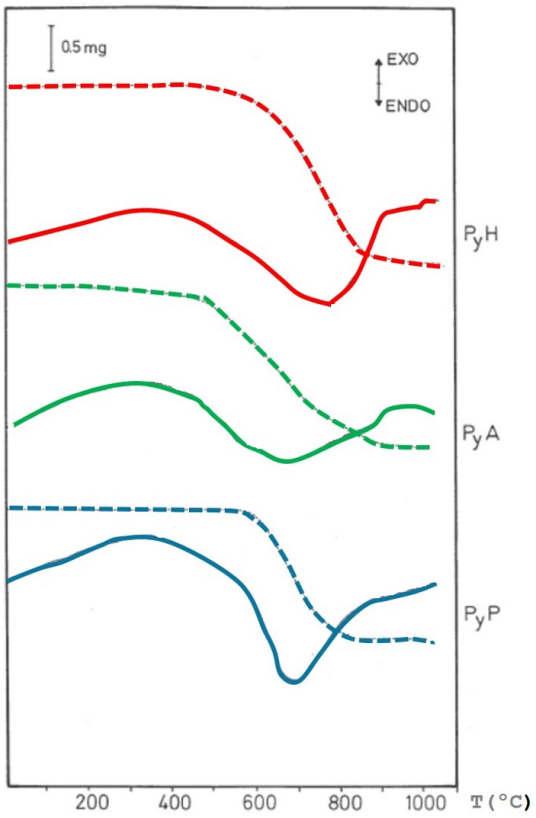

Figure 6. DTA-TG diagrams of pyrophyllite samples PyH, PyA, and PyP.

On the other hand, the DTA diagrams of the pyrophyllite samples show several variations. The broad endothermic effect is associated with the dehydroxylation of pyrophyllite in a wide range of temperatures. This effect is centered at ~760 °C for sample PyH, ~680 °C for sample PyA, and ~660 °C for sample PyP. These results, in general, agree with previous reported DTA diagrams of pyrophyllite samples in the literature [9,23,33,37,68,90,97,109].

It should be noted that a small exothermic effect was observed in sample PyH. This effect is associated with the 1:1 layered silicate kaolinite, identified as an impurity in this sample (Figure 2), taking into account the DTA curve of pure kaolinite [90,106,123,128]. If kaolinite is removed from this sample, this characteristic DTA effect disappeared [115]. In sample PyA, the broad endothermic DTA effect associated to kaolinite dehydroxylation (in the range 500–600 °C) overlapped with the broader endothermic DTA effect associated to pyrophyllite dehydroxylation, besides of the detection of an endothermic DTA effect characteristic of quartz phase transformation at ~573 °C [129]. All these features are in accordance with mineralogy as presented above (see Section 3.2). It must be emphasized that the dehydroxylation process is very much affected by the particle size of the pyrophyllite sample, as found by Pérez-Rodríguez et al. [109] in a previous study on dehydroxylation-rehydroxylation of pyrophyllite. These researchers separated several fractions of a sample of pyrophyllite by aqueous gravity sedimentation with different particle sizes. They found that the smaller the pyrophyllite particles, the lower the dehydroxylation temperature.

Mechanical treatment by grinding also influences the dehydroxylation of pyrophyllite at lower temperatures as compared to the original (unground) sample, as demonstrated by Sánchez-Soto et al. [104,123,130].

It can be mentioned a previous investigation on a pyrophyllite sample from Taining (Fujian Province, China) [88]. The authors of this study reported two stages in the TG curve (and two peaks in the corresponding first derivative or DTG curve) concerning: (a) first weight loss between 500 and 820 °C, associated to the dehydroxylation of pyrophyllite, approximately 5.19 wt. %, and (b) second weight loss of

0.46 wt. % between 820 °C and 900 °C ascribed to the dehydroxylation of pyrophyllite because the sample studied by these authors "has two hydroxyl groups" [88]. The present results (Figure 6), studying three pyrophyllite samples, are in disagreement with this assumption.

Previous studies on thermal decomposition of pyrophyllite samples of distinct geological origins proposed a two-step mass loss, associated to two DTA endothermic effects, during dehydroxylation. Nemecz [9] reported pyrophyllite samples with three-step mass loss associated to three distinct DTA endothermic effects with peaks centered at 540, 655, and 845 °C. In general, there is a variability in the thermal behaviour of pyrophyllite samples according to the literature. It has been proposed an intermediate partially dehydroxylated phase and the dehydroxylation of pyrophyllite is a two-stage process with a defined intermediate stage [105,109] and the presence of different possible intermediates during dehydroxylation of pyrophyllite [107,108]. There are pyrophyllite minerals with trans-vacant and cis-vacant structures, as well as cis- and trans-mixtures or interstratification of pyrophyllite phases [109]. However, the DTA-TG results presented in Figure 6 indicate a single step mass loss in the TG diagram and broad DTA effects in the pyrophyllite samples studied in the present work.

3.6. Thermo-Dilatometric Study

The thermo-dilatometry diagrams of the pyrophyllite samples (Figure 7) show an expansion effect above 500 °C, which goes parallel with the progressive dehydroxylation and elimination of structural water (Figure 6) by thermal treatment under dynamic conditions of heating. The maximum measured linear expansion is ~2% in samples PyH and PyP, being lower in sample PyA, taking into account the relative proportion of pyrophylite in all these samples (Figure 2). In contrast, thermo-dilatometry curves of kaolinite show an important contraction change in the temperature range 500–600 °C, associated to dehydroxylation and formation of "metakaolinite" [90] and a rapid contraction rate in the thermal curve from 700 to 1000 °C associated to the first stages of sintering [129]. Inoue and Okuda [131] indicated an abnormal expansion of pyrophyllite and sericite compacts during dehydroxylation. Other authors [68] reported 1.865% expansion by thermo-dilatometry of a raw pyrophyllite specimen heated at 1000 °C.

A plateau is observed in these pyrophyllite samples between ~700 and 1000–1100 °C, although it is at a lower temperature in the case of sample PyA. When dehydroxylation has been completed, and the samples are progressively heated, the thermo-dilatometric curve shows a slight contraction-expansion effect. It is followed by a fast contraction above 1100–1200 °C, being before and faster in sample PyA, which contains a lower relative content of pyrophyllite mixed with a proportion of quartz. This thermo-dilatometric change by heating is associated to the decomposition of dehydroxylated pyrophyllite formed by thermal treatment and subsequent formation and development of high-temperature phases. Finally, once the high-temperature phases are formed, sintering of the materials takes place, but it is very fast as the temperature increases, and a contraction associated to this process can be observed in the thermo-dilatometric curve. A similar feature using the same technique, although up to 1000 °C as maximum temperature, has been reported by Schomburg [132].

It should be noted that Shamim et al. [133] have studied the thermal "exfoliation" of pyrophyllite. These authors considered "exfoliation" as the process of "irreversible thermal expansion due to disarticulation of clay mineral layers". The sample was a well crystalline monoclinic pyrophyllite (2M1 polytype) [2,13,14] used in the preparation of triaxial porcelains [66]. However, Shamim et al. [133] used a monolithic block of pyrophyllite for studying this thermal exfoliation and deduced a kinetic pathway. In the present study, all the pyrophyllite samples were prepared as pellets using pressed powders for the thermo-dilatometric analysis.

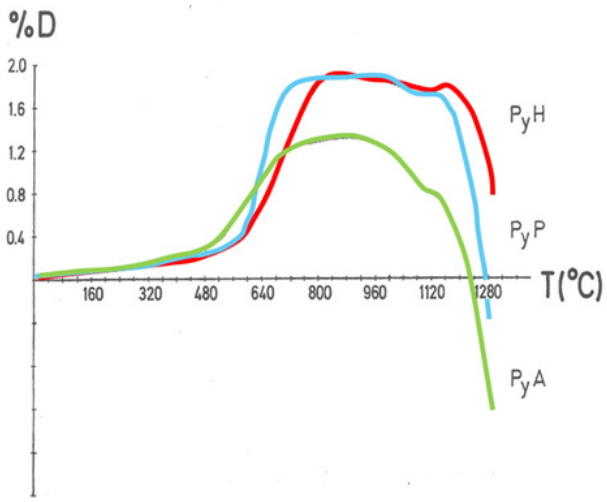

Figure 7. Thermo-dilatometric diagrams of pyrophyllite samples PyH, PyA, and PyP.

3.7. XRD Study of Thermally Treated Samples

All the pyrophyllite samples were subjected to several thermal treatments in air using a furnace and cooled, following the conditions described in Section 2.2. After these treatments, one part of the treated samples was ground and examined by XRD to investigate the changes experimented by identification of the crystalline phases. Thus, the main changes experimented by thermal treatments in sample PyH are presented in Figure 8. This pyrophyllite sample treated at 800 °C/24 h (Figure 8a) shows the characteristic X-ray patterns of dehydroxylated pyrophyllite [2,4], originated by reaction (1) as pointed out in the Introduction of this paper. There is a shift of the reflections with respect to the original (Figure 2). Thus, the interplanar distances (*d*-spacings) increase lightly, being determined as ~0.1 Å (1 Å = 0.1 nm). For instance, the 9.21 Å in original pyrophyllite (not-dehydroxylated) changes to 9.31 Å in the dehydroxylated phase; the *d*-spacing at 4.57 Å changes to 4.67 Å; the *d*-spacing at 3.05 Å changes to 3.11 Å, and so on. This effect is responsible of the expansion effect observed by thermo-dilatometry (Figure 7).

Dehydroxylated pyrophyllite, as a crystalline phase, is not destroyed by thermal treatment at 1100 °C/24 h of a fresh sample of pyrophyllite PyH (Figure 8). With this thermal treatment, small and weak mullite X-ray patterns begin to appear, associated with mullite nuclei, because this phase is not fully developed (Figure 8b). It seems like in kaolinite decomposed by thermal treatment [90,106,112,128,129], although in kaolinite the dehydroxylation produces an amorphous phase to X-rays, in contrast to pyrophyllite [2,4,90,95–100].

Pyrophyllite PyH treated at 1150 °C/24 h, produces mullite ($3Al_2O_3 \cdot 2SiO_2$) as a well-formed and crystallized phase according to the resolution of the X-ray patterns (Figure 8c). At the same time, cristobalite (SiO_2) can be identified in the sample by decomposition of dehydroxylated pyrophyllite and crystallization of amorphous silica. This amorphous phase is segregated in the process of formation and crystallization of mullite according to reaction (2), as pointed out in the Introduction. In that case, the coordination of Al changes from Al^{V} in dehydroxylated pyrophyllite to more estable Al^{VI} in mullite [90,100,104]. Further discussion on this subject, with a comparison between kaolinite (1:1 layered silicate) and pyrophyllite (2:1 layered silicate), has been performed by Moya et al. [90].

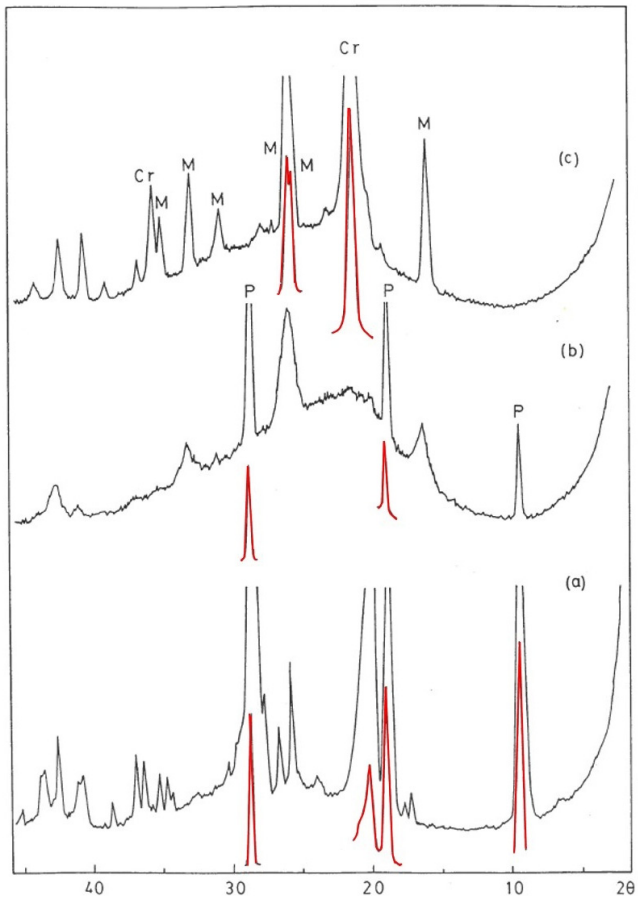

Figure 8. XRD of pyrophyllite sample PyH after several thermal treatments: (**a**) 800 °C/24 h; (**b**) 1100 °C/24 h, and (**c**) 1150 °C/24 h. P = Dehydroxylated Pyrophyllite; M = Mullite; Cr = Cristobalite. Red colours of some peaks indicate the exact position of the X-ray peaks in these XRD obtained under enhanced experimental conditions, because it was possible in the X-ray equipment to diminish the conditions to record the intensity of the peaks.

Mukhopadhyay et al. [66], in accordance with previous results by Wang et al. [105] using IR spectroscopy, suggested that the SiO_4 tetrahedral sheet structure still exists in the crystalline dehydroxylated pyrophyllite up to 900 °C. Thus, the 2:1 layered structure and Si–O–Al linkages remain in this phase with the formation of trigonal AlO_5 bi-pyramids as early proposed [2,4]. At 1100 °C dehydroxylated pyrophyllite decomposes into poorly ordered mullite, with a bonding rearrangement and a simultaneous release of SiO_2 as an amorphous phase. When impurities are present (Table 3), this amorphous phase, in fact, is forming a SiO_2-rich vitreous or glassy phase.

Table 3. Chemical analysis of pyrophyllite samples (calcined basis).

Composition (wt. %)	PyH	PyA	PyP	ZS	Theoretical Pyrophyllite
SiO_2	70.22	72.92	65.45	56.44	70.21
Al_2O_3	28.87	25.45	28.07	37.81	29.78
Fe_2O_3	0.21	0.25	0.08	0.66	-
TiO_2	0.10	0.10	6.01	1.60	-
CaO	0.09	0.09	0.15	0.38	-
MgO	0.01	0.03	0.06	0.24	-
Na_2O	0.10	0.15	0.08	0.49	-
K_2O	0.25	0.47	0.00	2.02	-
Total	99.85	99.46	99.90	99.64	99.99
Σ “oxides”	0.76	1.09	6.38	5.39	-

In summary, a prolonged thermal treatment produces the nucleation and formation of high-temperature phases, mullite and cristobalite, by decomposition of dehydroxylated pyrophyllite. Thus, it can be deduced that there are important kinetic effects in the thermal decomposition of pyrophyllite. In fact, Pérez-Rodríguez et al. [109], in a previous study on dehydroxylation-rehydroxylation of pyrophyllite, concluded that dehydroxylation of pyrophyllite is a kinetically driven process, with an activation energy (determined by the isoconversional method) of 224 ± 16 kJ/mol, being a value independent of the reaction fraction. Shamim et al. [134] performed a non-isothermal kinetic evaluation of pyrophyllite dehydroxylation using the same sample of pyrophyllite studied by Mukhopadhyay et al. [68], in fact a sericitic/muscovitic mineral ($Na_2O + K_2O$ = 2.68 wt. % containing 59.51 wt. % of SiO_2 and 30.43 wt. % of Al_2O_3 compare with results included in Table 1), with pyrophyllite. Shamim et al. [134] reported an activation energy of 159 kJ/mol, considering a single stage diffusion reaction model. As in kaolinite, the dehydroxylation process precedes mullitization [71,90,128,129], but in the case of pyrophyllite the dehydroxylated phase is a crystalline phase [4,90,93–105,107–109].

On the other hand, the DTA diagram of the pyrophyllite sample PyH treated at 1150 °C (Figure 9) shows an endothermal effect, centered at 180 °C, associated to the inversion of cristobalite (α) to cristobalite (β), a first order transition without breaking of bonds or creation of defects. Previous investigations indicated that the cristobalite α-β inversion can be produced between 160 and 275 °C according to the crystal features [135–139]. It may be detrimental to the refractories containing cristobalite [135]. Cristobalite can be formed at 1100 °C [137]. In the present study, however, cristobalite is not detected after thermal treatment at 1100 °C/24 h, but it is detected at 1150 °C/24 h (Figure 8). Thus, it can be assumed that the effect of the Si–Al matrix is an important factor in the formation and development of cristobalite, from amorphous segregated silica when mullite is formed by thermal decomposition of dehydroxylated pyrophyllite, according to reaction (2).

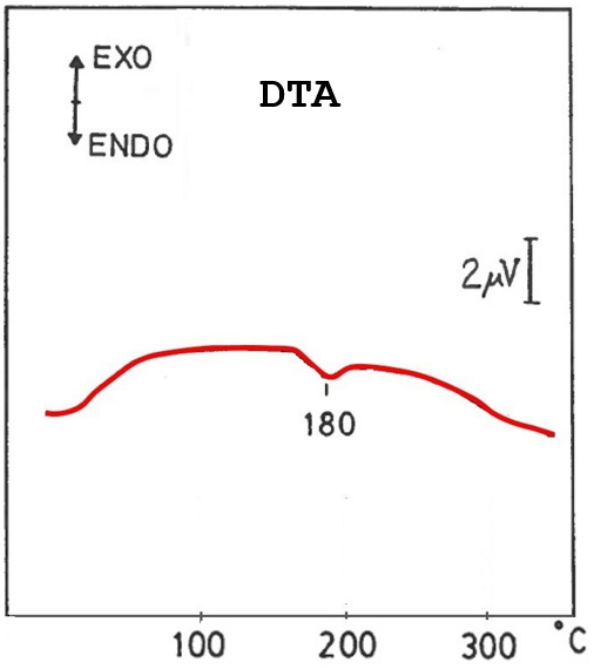

Figure 9. DTA diagram of pyrophyllite sample PyH after thermal treatment at 1150 °C/24 h.

It should be noted that several studies have reported on the temperature dependence of the cristobalite α-β inversion starting by high-purity quartz or glass compositions heated at temperatures between 1100 and 1700 °C, with and without addition of a mineralizer. The results were explained in terms of the degree of

order of the cristobalite structure [137]. The present investigation is the first time where a thermal study by DTA of cristobalite, formed from thermal decomposition of dehydroxylated pyrophyllite, is reported.

A mitigation strategy to avoid the presence of cristobalite, detrimental for ceramics and refractories, is the addition of alumina (for instance, as α-Al_2O_3, corundum, or as aluminium hydroxide, gibbsite). Thus, alumina reacts with an excess of silica originating from the thermal decomposition of dehydroxylated pyrophyllite and can originate a secondary mullite by thermal treatment at higher temperatures than 1300 °C. Then, high-mullite refractory materials can be obtained where the stoichiometry composition of mullite ($3Al_2O_3 \cdot 2SiO_2$) or Al_2O_3/SiO_2 with a molar ratio of 1.5. It is favored that the heating treatments be at 1550–1600 °C. In the case of kaolinite, the molar percentage of SiO_2 is 66.66 mol %, being higher in the case of pyrophyllite (80 mol. %). Thus, more Al_2O_3 must be added for pyrophyllite to yield more mullite by reaction with SiO_2. For instance, it was studied in a previous research using pyrophyllite-gibbsite mixtures and compared with kaolin-gibbsite mixtures [74]. Pyrophyllite raw materials can also be used in the preparation of triaxial porcelains and the formation of cristobalite is not produced [66–68]. These kinds of studies, using the pyrophyllite samples PyH, PyA, PyP, and ZS, will be a matter for future research.

On the other hand, thermal treatment at 1150 °C/24 h performed in the case of pyrophyllite clay sample ZS studied by XRD shows well-crystallized mullite (Figure 10). In this sample, mullite is associated with the thermal decomposition of the layered silicates identified by XRD (Figure 3): kaolinite, muscovite mica/illite or sericite, and pyrophyllite. It can be considered a sericite clay with pyrophyllite, which decomposes by thermal treatment, yielding mullite and cristobalite. In this sense, Reddy and Kim [69] and Wang et al. [70] have emphasized the role of sericite as an additive or sintering aid in composites and the preparation of high-porosity mullite ceramics.

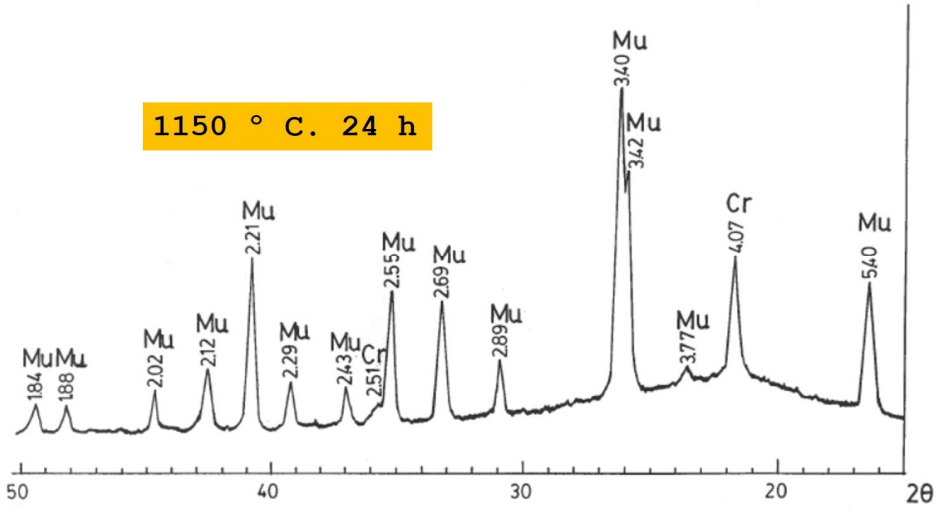

Figure 10. XRD diagram of pyrophyllite clay sample ZS after thermal treatment at 1150 °C/24 h. Mu = Mullite; Cr = Cristobalite. The numbers are selected *d*-spacings of the mineral phases in Å (1 Å = 0.1 nm).

Furthermore, a hump, centered at ~22° 2θ, is detected in all the XRD diagrams (Figures 8 and 10), being associated to an amorphous phase segregated when mullite progressively appears by thermal treatments of all these pyrophyllite samples. Cristobalite (in fact, β-cristobalite) is formed from the amorphous phase, although in the case of pyrophyllite clay ZS, the amorphous phase seems better associated to a vitreous or glassy phase (amorphous to X-rays) according to the content of impurities, distinct of silica and alumina, present in this sample (Table 1). A deep analysis of the XRD patterns of thermally treated pyrophyllites, as presented in Figures 8 and 10, allow determine that the mullite has an orthorhombic structure [140] according to the characteristic doublet formed by the (hkl) planes (120) and (210) at 3.42 and 3.40 Å (1 Å = 0.1 nm), with relative intensities 95 and 100, respectively.

3.8. SEM Study of Thermally Treated Samples

The pyrophyllite samples thermally treated, studied by XRD (Figures 8 and 10), as described in the precedent subsection, were also examined by SEM. Figure 11 shows some selected SEM micrographs. Figure 11a presents the morphology of sample PyH treated at 1100 °C/24 h, were flat particles can be observed, being associated to dehydroxylated pyrophyllite (Figure 8). Differences between original and thermally treated pyrophyllite samples up to 1100 °C cannot be found. However, Figure 11b corresponds to the same pyrophyllite sample PyH treated at 1150 °C/24 h, where the microstructure has lost the flat appearance although some small flat particles can be observed. Besides these features, some sintered and bonded particles can be observed. These particles must be associated with mullite and cristobalite, crystalline phases identified by XRD in the thermally treated sample (Figure 8c). A similar effect, although more intense and extended, can be observed in pyrophyllite clay sample ZS thermally treated at 1150 °C/24 h (Figure 11c), where sintering with formation of coalescent particles and some pores can be observed. In this sample, mullite and cristobalite are well developped crystalline phases besides the presence of a glassy or vitreous phase, according to the XRD results (Figure 10).

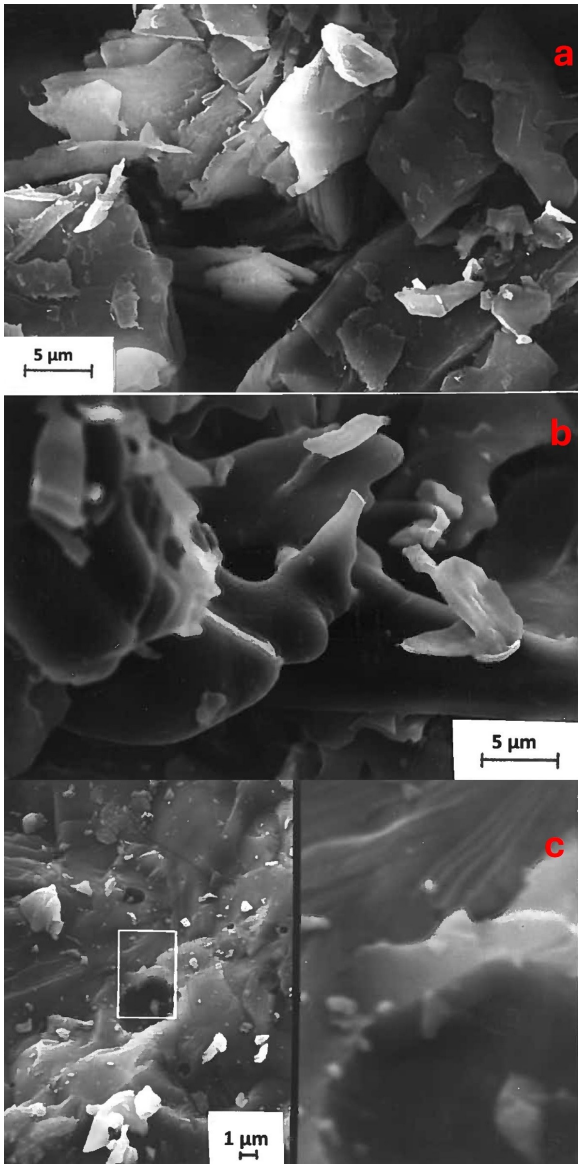

Figure 11. (**a**) Selected SEM micrographs of the pyrophyllite sample PyH after thermal treatment at 1100 °C/24 h, (**b**) the same sample PyH at 1150 °C/24 h, and (**c**) the pyrophyllite clay sample ZS after thermal treatment at 1150 °C/24 h, showing a particular detail at high magnification.

3.9. XRD and SEM Study of Pressed Samples After Thermal Treatment at 1300 °C

In this step of the present work, it was interesting to study the samples with pyrophyllite as the main crystalline phase (PyH, PyA, and PyP) at higher temperatures than precedent investigation as described above. The maximum temperature reached in the thermo-dilatometric runs has been selected for this study and sintering was starting (Figure 7). The pressed samples were subjected to two cycles of thermal treatment at 1300 °C using the SiC furnace of the thermo-dilatometer. Figure 12 presents the XRD diagrams of these thermally treated samples. It can be observed that mullite and cristobalite are well-developed crystalline phases in pyrophyllite samples PyH and PyA. In the sample PyP, as in the precedents, these phases are being formed from thermal decomposition of dehydroxylated pyrophyllite, although the conversion is relatively slower. Quartz is still present in sample PyA after the thermal treatment. Rutile is identified in sample PyP, as in the original (unheated) sample (Figure 2).

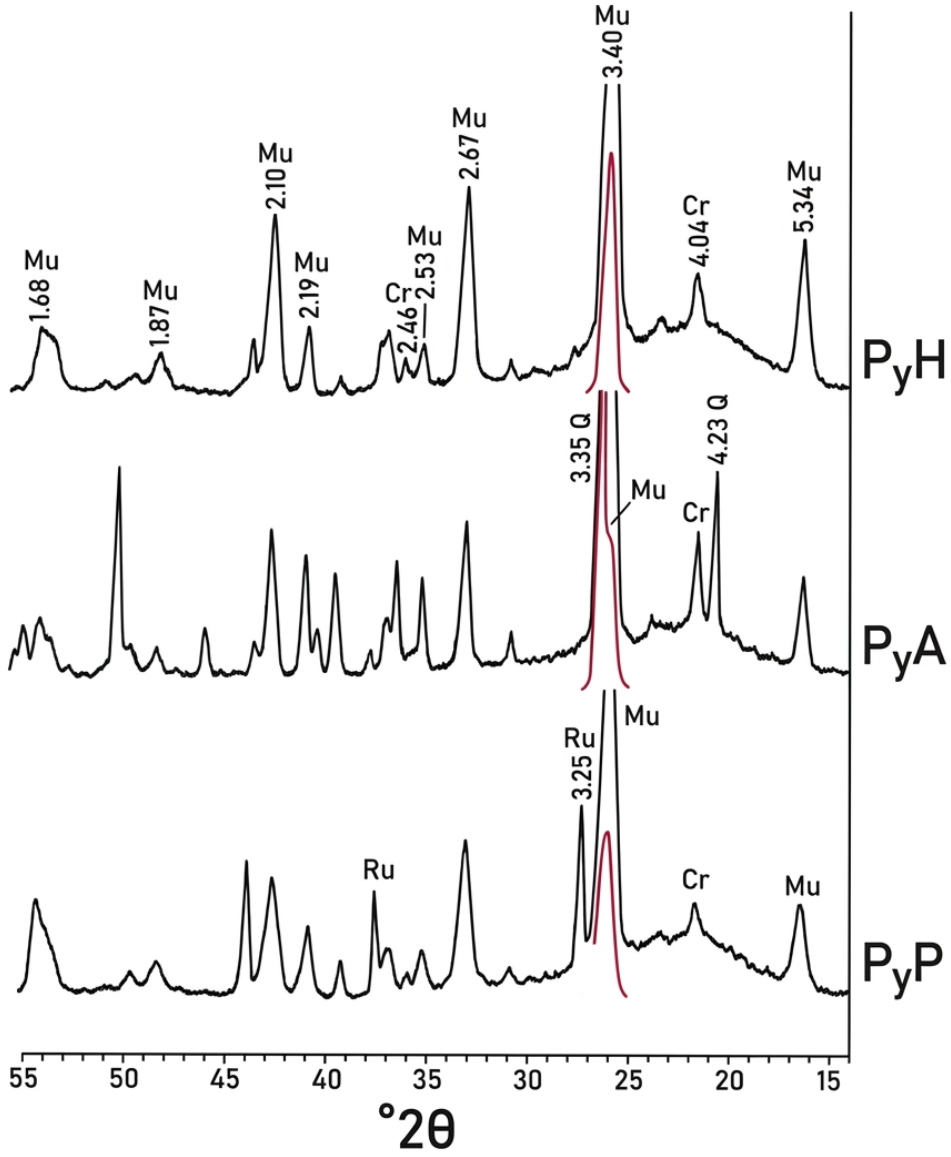

Figure 12. XRD diagrams of pyrophyllite samples PyH, PyA and PyP prepared as pressed pellets for thermo-dilatometric analysis (Figure 7) after two cycles at 1300 °C in the furnace of the thermo-dilatometric equipment. Mu = Mullite; Q = Quartz; Cr = Cristobalite; Ru = Rutile. The numbers are selected *d*-spacings of the mineral phases in Å (1 Å = 0.1 nm). Red colours of some peaks indicate the exact position of the X-ray peaks in these XRD obtained under enhanced experimental conditions, because it was possible in the X-ray equipment to diminish the conditions to record the intensity of the peaks. Red colours of some peaks indicate the exact position of the X-ray peaks in these XRD obtained under enhanced experimental conditions.

It is clear that the existence of impurities (as seen in Table 3) influences the thermal behaviour by the formation of a glassy phase (amorphous to X-rays), being liquid at high temperature. It is responsible of the hump observed in the XRD diagrams at ~22° 2θ. In this sense, Table 3 shows the chemical analysis of all the pyrophyllite samples on a calcined basis, where the sum of oxides distinct of SiO_2 and Al_2O_3 is relatively higher in pyrophyllite samples PyP and ZS. However, the pyrophyllite clay sample contains other layered silicates besides of pyrophyllite (Figure 3). Sample PyP contains 6.01 wt. % of TiO_2 and, hence, the value of the sum of the oxides could not be representative of the current situation in other pyrophyllite samples. Samples PyH and PyA present a content of oxides, distinct of silica and alumina, lower than that found in other pyrophyllite samples as pointed out in the discussion of chemical results (Section 3.1), being these values representative. In consequence, the refractory prepared using PyH, PyA, and even ZS would be of interest.

The predictions deduced from the K_2O–Al_2O_3–SiO_2 ternary equilibrium phase diagram [141] and the analysis of the effect of vitreous phase on mullite [142] are in agreement with the behaviour observed in these samples, with formation of more amount of liquid phase (vitreous or glassy phase after cooling the samples at room temperature) as increasing temperature if there is a larger proportion of impurities in these samples. It may be of interest in the preparation of vitrified mullite ceramics with moderate resistance to high temperatures, as demonstrated in a previous investigation [143].

The case of pyrophyllite PyP is distinct as compared with samples PyH and PyA because this sample contains TiO_2 and it must be considered the TiO_2–Al_2O_3–SiO_2 ternary equilibrium phase diagram [144,145]. The oxide TiO_2 could originate a solid solution with mullite at high-temperature and even the formation of aluminum titanate would be possible although in a low relative proportion [144,145]. It should be noted that a previous analysis of the sintering behaviour and the vitrification process of a pyrophyllite clay containing sericite and kaolinite, with application as raw ceramic material, has been performed [146], being related to other raw clays with a wide range of chemical composition [147]. The ultimate goal of these studies was to estimate the optimum firing conditions concerning the fabrication of structural ceramic materials obtained from these raw clays. It is important to remark that sericite is a “natural flux”, being interesting because raw ceramic materials with high sericite content and fine particles produce the formation of mullite at relatively low temperatures (~1000 °C) with an improvement in energy savings according to precedent studies [25,65,69–71].

Finally, it was of relevant interest a SEM examination of these pressed and thermally treated pyrophyllite samples. Previously, these samples were subjected to chemical etching using 20 vol. % HF [146] to remove the glassy/vitrified phase and other phases (such as quartz). Figure 13 includes selected SEM micrographs. It can be seen the long-elongated crystals of mullite, in particular in sample PyP (Figure 13c), forming a felt of crystals, sometimes as needle-like crystals (Figure 13a,b). Thus, mullite crystallization can produce an interlocking dense microstructure in these pyrophyllite samples that have been thermally treated.

In samples PyH and PyA there are relicts of glassy phase not eliminated by chemical etching. EDX analysis confirmed the mullite composition of all these crystals because only Al and Si are detected. This microstructure is characteristic of ceramic materials containing mullite [32,66–68,71,74,140,142,143,146,148]. These results are of interest to the preparation of high-temperature ceramics and mullite refractory materials using these pyrophyllite samples. It will be the subject of future investigations.

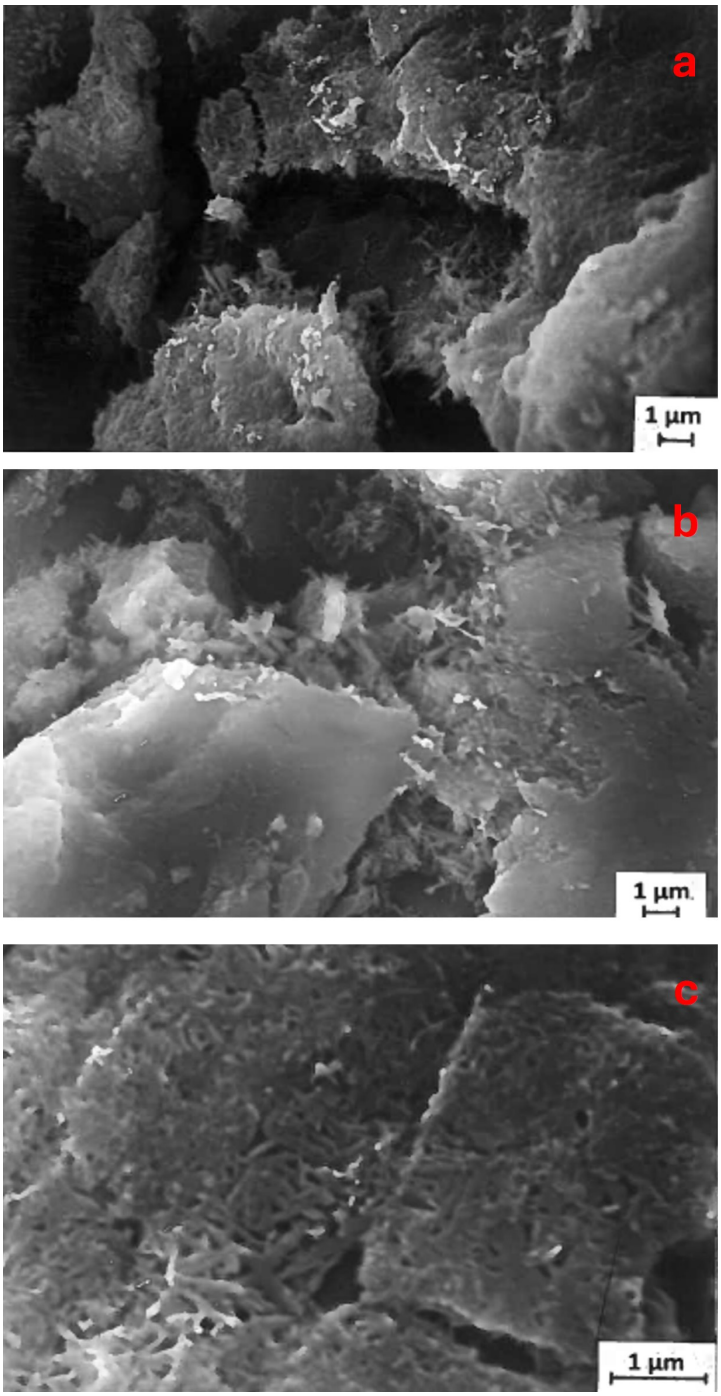

Figure 13. Selected SEM micrographs of pyrophyllite samples prepared as pressed pellets for thermo-dilatometric analysis after two cycles at 1300 °C examined in fractured surfaces after chemical etching using 20 vol. % HF: (**a**) Pyrophyllite sample PyH; (**b**) Pyrophyllite sample PyA, and (**c**) Pyrophyllite sample PyP.

4. Summary and Conclusions

The 2:1 layered silicate pyrophyllite, as the main crystalline phase, has been identified in all the samples (PyH, PyA, PyP and ZS) by XRD, although a relatively minor proportion of other mineral phases are present, in general, layered silicates (kaolinite, muscovite/illite or sericite, chlorite). Polytype identification in the samples was difficult, although mixtures of polytypes 1Tc and 2M are present in all samples, with polytype 1Tc predominant in one sample (PyP). The samples studied in this investigation showed high-pyrophyllite contents according to the chemical analyses, with minor amounts of impurities (Table 1) and [SiO_2/Al_2O_3] molar ratios close to the theoretical value of pyrophyllite (4.00). Besides this, a

sample (PyA) contains quartz as a secondary mineral phase, and other pyrophyllite sample (PyP) contains a minor secondary mineral phase, rutile, as a residual product of the chemical attack to obtain a purified pyrophyllite. These mineralogical and chemical features have been confirmed by SEM-EDX.

The specific surface areas of all these samples were found to be lower than 6 m^2/g, except the pyrophyllite clay ZS. Then, the values of geometrical particle sizes, assuming spherical shapes, were estimated to be lower than 3.5 μm in all these pyrophyllite samples, being the lowest in sample PyA (Table 2) because this sample was ground by the supplier. The pyrophyllite clay sample did not agree with all these features because it contains pyrophyllite and other layered silicates in relatively high proportions (kaolinite and muscovite/illite or sericite) as compared with samples with high pyrophyllite contents.

Thermal analysis (DTA-TG and dilatometry) allowed us to investigate the dehydroxylation process of pyrophyllite under dynamic conditions of heating. This process occurred with an expansion effect above 500 °C, with a progressive weight loss by TG (total lower than 6 wt. % except in the pyrophyllite clay sample), and a broad endothermic effect by DTA centered at 760 °C, 680 °C, and 660 °C for the pyrophyllite samples PyH, PyA, and PyP, respectively. The thermo-dilatometry study indicated that contraction-expansion effects are produced by progressive heating, under dynamics conditions, with a fast contraction by sintering in the samples above 1100–1200 °C. This contraction was faster in the case of the pyrophyllite sample PyA, which contains quartz. These changes, recorded under dynamic heating conditions, were associated with the thermal decomposition of dehydroxylated pyrophyllite, forming the high-temperature phases mullite and cristobalite, as revealed by XRD.

The treatments of all the pyrophyllite samples under static conditions at 800 °C, 1100 °C, and 1150 °C/24 h revealed: (a) the formation of dehydroxylated pyrophyllite, with small variations of *d*-spacings as compared with the normal (undehydroxylated) pyrophyllite, and (b) its thermal decomposition by heating to form mullite. The formation of dehydroxylated pyrophyllite as crystalline phase in the samples was established after 1050 °C by XRD and its permanency above this temperature, with little changes in morphological features, as revealed the SEM study.

In the pyrophyllite samples under two cycles of thermo-dilatometry at 1300 °C XRD evidenced the formation and crystallization of mullite ($3Al_2O_3 \cdot 2SiO_2$) as high-temperature phase. This phase is produced with a progressive destruction of dehydroxylated pyrophyllite. Cristobalite (SiO_2) was formed by crystallization of the amorphous silica which is segregated in the solid-state reaction of formation of mullite. A kinetic effect in the development of the crystalline phases has been deduced from these results. The humps observed by XRD in the heated samples were attributed to the presence of an amorphous phase, being associated to a vitreous or glassy phase (liquid at high temperature) when the content of impurities is relatively high (Table 3). It is particularly relevant in the case of the pyrophyllite clay.

The treatment at 1300 °C of the pyrophyllite samples as mentioned above produces a new microstructure, as revealed by SEM after chemical etching using HF to remove the possible amorphous phase and quartz, with identification of elongated and needle-like crystals of mullite forming sometimes a tupid felt. The formation and crystallization of mullite from pyrophyllite are interesting for high-temperature applications, for instance, as ceramics and refractory materials based on mullite. However, the presence of cristobalite must be avoided because this crystalline form of silica can be detrimental for these applications.

Acknowledgments

The authors want to dedicate this work to José L. Pérez-Rodríguez at the Institute of Materials Science of Sevilla (CSIC-University of Sevilla), now retired, with occasion of his 87th birthday. The experimental contribution of M. Macías to determine the specific surface areas of the samples is acknowledged.

Author Contributions

P.J.S.-S.: Conceptualization, Investigation, Methodology, Funding acquisition, Formal analysis, Data curation, Supervision, Writing—original draft, Writing—review & editing. E.G.: Conceptualization, Investigation, Writing—original draft, Writing—review & editing, Supervision, Formal analysis, Visualization, Validation. V.G.-G.: Investigation, Methodology, Writing—review & editing. J.A.S.-G.: Software, Data curation, Writing—review & editing. L.P.-V.: Writing—review & editing, Supervision, Data curation. S.M.-M.: Investigation, Formal analysis, Writing—review & editing. All authors have read and agreed this original paper submitted for revision and publication in High Temperature Materials.

Ethics Statement

Not applicable.

Informed Consent Statement

Not applicable.

Data Availability Statement

The readers are informed about the accessibility of research data linked to this paper writing to the corresponding authors.

Funding

This work has been carried out as part of the projects financially supported by Research Groups TEP 204 and AGR 107 through Andalusian Regional Government.

Declaration of Competing Interest

The authors declare that they have no known competing financial interest or personal relationships that could have appeared to influence the work reported in this paper.

References

1. Rayner JH, Brown G. Structure of pyrophyllite. *Clays Clay Miner.* **1964**, *13*, 73–84. DOI:10.1346/CCMN.1964.0130108
2. Brindley GW, Wardle R. Monoclinic and triclinic forms of pyrophyllite and pyrophyllite anhidride. *Am. Miner.* **1970**, *55*, 1259–1272. Available online: https://pubs.geoscienceworld.org/msa/ammin/article-abstract/55/7-8/1259/540691 (accessed on 6 March 2026).
3. Ward W, Phillips JM. Calculated lamellar binding I. Van der Waals bonding in talc and pyrophyllite. *Surface Sci.* **1971**, *25*, 379–384. DOI:10.1016/0039-6028(71)90258-5
4. Wardle R, Brindley GW. The crystal structures of pyrophyllite, 1Te, and of its dehydroxylate. *Am. Miner.* **1972**, *57*, 732–750. Available online: https://pubs.geoscienceworld.org/msa/ammin/article-abstract/57/5-6/732/542635 (accessed on 6 March 2026).
5. Giese RF. Interlayer bonding in talc and pyrophyllite. *Clays Clay Miner.* **1975**, *23*, 165–166. DOI:10.1346/CCMN.1975.0230218
6. Alcover JF, Giese RF. Energie de liaison des feuillets de talc, pyrophyllite, muscovite et phlogopite. *Clay Miner.* **1986**, *21*, 159–169. DOI:10.1180/claymin.1986.021.2.05
7. Brindley GW, Brown G. (Eds). *Crystal Structures of Clay Minerals and Their X-Ray Identification*; Mineralogical Society: London, UK, 1980.
8. Lee JH, Guggenheim S. Single crystal X-ray refinement of pyrophyllite 1Tc. *Am. Miner.* **1981**, *66*, 350–357. Available online: https://pubs.geoscienceworld.org/msa/ammin/article-abstract/66/3-4/350/41261 (accessed on 6 March 2026).
9. Nemecz E. Pyrophyllite 1Tc occurrence at Pázmand (Hungary) in fluorine activized environment. *Acta Geol. Hung.* **1984**, *27*, 191–202. Available online: https://pascal-francis.inist.fr/vibad/index.php?action=getRecordDetail&idt=8443534 (accessed on 6 March 2026).

10. Newman ACD. (Ed). *Chemistry of Clays and Clay Minerals*; Monograph 6; Mineralogical Society: London, UK, 1986.
11. Eberl D. Synthesis of pyrophyllite polytypes and mixed layers. *Am. Miner.* **1979**, *64*, 1091–1096. Available online: https://pubs.geoscienceworld.org/msa/ammin/article-abstract/64/9-10/1091/41087 (accessed on 6 March 2026).
12. Rosenberg PE, Cliff G. The formation of pyrophyllite solid solutions. *Am. Miner.* **1980**, *65*, 1217–1219. Available online: https://pubs.geoscienceworld.org/msa/ammin/article-abstract/65/11-12/1217/104702 (accessed on 6 March 2026).
13. Weiss Z, Durovic S. Polytypism of pyrophyllite and talc. II. Classification and X-ray identification of MDO polytypes. *Silikáty* **1984**, *28*, 289–309. Available online: https://pascal-francis.inist.fr/vibad/index.php?action=getRecordDetail&idt=8929195 (accessed on 6 March 2026).
14. Wiéwiora A, Sánchez-Soto PJ, Avilés MA, Justo A, Pérez-Rodríguez JL. Effect of dry grinding and leaching on polytypic structure of pyrophyllite. *Appl. Clay Sci.* **1993**, *8*, 261–282. DOI:10.1016/0169-1317(93)90008-O
15. Misra ML, Upadhyaya VG. Use of pyrophyllite from Harmirpur in refractory enamels. *Trans. Indian Ceram. Soc.* **1960**, *19*, 67–69. DOI:10.1080/0371750X.1960.10855392
16. Loughnan IC, Ward CR. Pyrophyllite-bearing Flint clay from the Cambewarra area, New South Wales. *Clay Miner.* **1971**, *9*, 83–95. DOI:10.1180/claymin.1971.009.1.06
17. Abdrakhimova ES. Physicochemical studies of pyrophyllite of the Nikols'sk deposit. *Refract. Ind. Ceram.***2010**, *51*, 6–8. DOI:10.1007/s11148-010-9244-2
18. Bowman R, Tauber E. Potential applications of two high grade kaolinitic clays and one pyrophyllite deposits. *J. Aust. Ceram. Soc.* **1979**, *15*, 5–8. Available online: https://pascal-francis.inist.fr/vibad/index.php?action=getRecordDetail&idt=PASCAL8060020344 (accessed on 6 March 2026).
19. Nichol D. Pyrophyllite operations at Pambula, Australia. *Ind. Miner.* **1983**, *194*, 31–35. Available online: https://cir.nii.ac.jp/crid/1572543025079192448 (accessed on 6 March 2026).
20. Soirat M. Argiles d'Afrique du nord et possibilités d'utilisation de la pyrophyllite. *L'Ind. Ceram.* **1976**, *698*, 599–604. Available online: https://pascal-francis.inist.fr/vibad/index.php?action=getRecordDetail&idt=PASCAL7688007181 (accessed on 6 March 2026).
21. Bentayeb A, Amouric M, Olives J, Dekayir A, Nadiri A. XRD and HRTEM characterization of pyrophyllite from Morocco and its posible applications. *Appl. Clay Sci.* **2003**, *22*, 211–221. DOI:10.1016/S0169-1317(03)00066-8
22. Sykes ML, Moody JB. Pyrophyllite and metamorphism in the Caroline slate belt. *Am. Miner.* **1978**, *63*, 96–108. Available online: https://pubs.geoscienceworld.org/msa/ammin/article-abstract/63/1-2/96/40872 (accessed on 6 March 2026).
23. Swindale LD, Hughes IR. Hydrothermal association of pyrophyllite, kaolinite, diaspore, dickite and quartz in the Coromandel area, New Zealand. *New Zealand J. Geol. Geophys.* **1968**, *11*, 1163–1183. DOI:10.1080/00288306.1968.10420245
24. Galán Huertos E, Martín Vivaldi JL. Caolines españoles: Geología, Mineralogía y Génesis. Parte IV. Depósitos Paleozoicos, Neógenos y Cuaternarios. *Bol. Soc. Esp. Ceram. Vidr.* **1974**, *13*, 523–546. Available online: https://pascal-francis.inist.fr/vibad/index.php?action=getRecordDetail&idt=PASCALGEODEBRGM7520062293 (accessed on 6 March 2026).
25. Espinosa de los Monteros J, Alvarez Estrada D, Morales Poyato F, del Río Sánchez MA. Arcillas sericíticas, nuevas materias primas cerámicas. *Bol. Soc. Esp. Ceram. Vidr.* **1978**, *17*, 73–78. Available online: https://dialnet.unirioja.es/servlet/articulo?codigo=7715774 (accessed on 6 March 2026).
26. Espinosa de los Monteros J, Alvarez Estrada D, de Aza Pendás S, Morales Poyato F. Pastas de cordierita y de cordierita-mullita obtenidas a partir de arcillas sericíticas. *Bol. Soc. Esp. Ceram. Vidr.* **1979**, *18*, 149–155. Available online: https://dialnet.unirioja.es/servlet/articulo?codigo=7734169 (accessed on 6 March 2026).
27. Bellinfante N, Tirado Coello JL, Paneque G. Propiedades técnicas de las arcillas de un yacimiento de Hinojosa del Duque (Córdoba). *Bol. Soc. Esp. Ceram. Vidr.* **1982**, *21*, 123–125. Available online: https://idus.us.es/bitstreams/72c28ec6-d799-43c2-8f8d-a66bd353b915/download (accessed on 6 March 2026).
28. Ullrich B, Lesch L. Pyrophillit. *Silikattechnik* **1987**, *38*, 274–275.
29. Zalba PE. Clay deposits of Las Aguilas formation Barker, Buenos Aires province, Argentina. *Clays Clay Miner.* **1979**, *27*, 433–439. DOI:10.1346/CCMN.1979.0270607
30. Mukherji SF. Importance of pyrophyllite in ceramic industry. *Indian Ceram.* **1983**, *26*, 123–125.
31. Galán Huertos E. Posibilidades de utilización de materias primas españolas en la fabricación de refractarios silicoaluminosos y de alta alúmina. *Bol. Soc. Esp. Ceram. Vidr.* **1981**, *20*, 33–39. Available online: https://dialnet.unirioja.es/servlet/articulo?codigo=7790304 (accessed on 6 March 2026).
32. Sánchez-Soto PJ, Justo A, Jiménez de Haro MC, Pérez-Rodríguez JL, Raigón M, Pascual J. Caracterización y propiedades cerámicas de una pizarra alumínica que contiene pirofilita. *Bol. Soc. Esp. Ceram. Vidr.* **1994**, *33*, 199–205. Available online: https://www.academia.edu/download/86349787/199433199.pdf (accessed on 6 March 2026).

33. Sánchez-Soto PJ, Pérez-Rodríguez JL. Características generales, propiedades, yacimientos y aplicaciones de pirofilita. I: Estructura, síntesis y características térmicas. *Bol. Soc. Esp. Ceram. Vidr.* **1998**, *37*, 285–289. Available online: https://digital.csic.es/handle/10261/15822 (accessed on 6 March 2026).
34. Sánchez-Soto PJ, Pérez-Rodríguez JL. Características generales, propiedades, yacimientos y aplicaciones de pirofilita. II: Yacimientos, aplicaciones y utilización como materia prima cerámica. *Bol. Soc. Esp. Ceram. Vidr.* **1998**, *37*, 359–368. Available online: https://digital.csic.es/handle/10261/15746 (accessed on 6 March 2026).
35. Zaykov VV, Udachin VN. Pyrophyllite and pyrophyllite raw materials in the sulfide-bearing areas of the Urals. *Appl. Clay Sci.* **1994**, *8*, 417–435. DOI:10.1016/0169-1317(94)90037-X
36. Sinyakovskaya I, Zaykov V, Kitagawa R. Types of Pyrophyllite Deposits in Foldbelts. *Resour. Geol.* **2005**, *4*, 405–418. DOI:10.1111/j.1751-3928.2005.tb00261.x
37. Ali MA, Ahmed HAM, Ahmed HM, Hefni M. Pyrophyllite: An Economical Mineral for Different Industrial Applications. *Appl. Sci.* **2021**, *11*, 11357. DOI:10.3390/app112311357
38. Ali MA, Ahmed HAM. Chemical and Mineralogical Characterization of Saudi-Pyrophyllite ore and its potential applications. *Arab Gulf J. Sci. Res.* **2022**, *39*, 1–18. DOI:10.51758/AGJSR-01-2021-0001
39. Hayashi H, Koshi K, Hamada A, Sakabe H. Structural change of pyrophyllite by grinding and its effect on toxicity of the cell. *Clay Sci.* **1962**, *1*, 99–108. Available online: https://www.jstage.jst.go.jp/article/jcssjclayscience1960/1/5/1_5_99/_article/-char/ja/ (accessed on 6 March 2026).
40. Morisaki H. Effect of solid-liquid interface on metabolic activity of *Escherichia Coli*. *J. Gen. Appl. Microbiol.* **1983**, *29*, 195–204. DOI:10.2323/jgam.29.195
41. Gorbey FW, Caplan PE, McKinnery WN, Cooper TC. Pyrophyllite dust control in the wall and floor tile industry. *Am. Ceram. Soc. Bull.* **1986**, *65*, 755–759. Available online: https://pascal-francis.inist.fr/vibad/index.php?action=getRecordDetail&idt=8800104 (accessed on 6 March 2026).
42. Paraš S, Paspalj J, Baghdad K, Janković O, Gajanin R, Massiani P, et al. Biocompatibility of nano/micro-sized pyrophyllite particles by pulmo, liver, kidney and gastric mucosis cells. *J. Mater. Sci. Mater. Med.* **2024**, *35*, 30. DOI:10.1007/s10856-024-06793-z
43. Dryagileva RI, Ivaniva TS, Kantka NA, Rosovitskii VT, Daisko PV. Polymerization of styrene on pyrophyllite as a method for its modification. *Plast. Massy* **1986**, *4*, 4–6.
44. Wang S, Li X, Ren K, Huang R, Lei G, Shen L, et al. Surface modification of pyrophyllite for optimizing properties of castor oil-based polyurethane composite and its application in controlled-release fertilizer. *Arab. J. Chem.* **2023**, *16*, 104400. DOI:10.1016/j.arabjc.2022.104400
45. Ruiz-Hitzky E, Casal B. Epoxide rearrangements on mineral and silica-alumina surfaces. *J. Catal.* **1985**, *92*, 291–295. DOI:10.1016/0021-9517(85)90263-5
46. El Gaidoumi A, Doña-Rodríguez JM, Pulido Melián E, González-Díaz OM, Navío JA, El Bali B. Catalytic efficiency of Cu-supported pyrophyllite in heterogenous catalytic oxidation of phenol. *Arabian J. Sci. Eng.* **2019**, *44*, 6313–6325. DOI:10.1007/s13369-019-03757-2
47. Erdermoğlu M, Erdermoğlu S, Sayilkan F, Akarsu M, Şener Ş, Sayilkan H. Organo-functional modified pyrophyllite: Preparation, reparation, characterisation and Pb(II) ion adsorption property. *Appl. Clay Sci.* **2004**, *27*, 41–52. DOI:10.1016/j.clay.2003.12.005
48. Zhang J, Zhou Y, Jiang M, Li J, Sheng J. Removal of methylene blue from aqueous solution by adsorption on pyrophyllite. *J. Mol. Liq.* **2015**, *209*, 267–271. DOI:10.1016/j.molliq.2015.05.056
49. Murtić S, Zahirović Ć, Karić L, Jurković J, Ćivić H, Sijahović E. Use of pyrophyllite as soil conditioner in lettuce production. *Nat. Environ. Pollut. Technol.* **2020**, *19*, 355–359. Available online: https://www.researchgate.net/profile/Cerima-Zahirovic-Sinanovic/publication/339602167_Use_of_Pyrophyllite_as_Soil_Conditioner_in_Lettuce_Production/links/673f9e0f27661f7ae6243e80/Use-of-Pyrophyllite-as-Soil-Conditioner-in-Lettuce-Production.pdf (accessed on 6 March 2026).
50. Hasanbehović E, Huremović J, Žero S. Adsorption capacity of nitrate from artificial fertilizers and soil on pyrophyllite. *Int. J. Environ. Sci. Technol.* **2021**, *18*, 3731–3738. DOI:10.1007/s13762-021-03135-2
51. Jeong Y, Lee S, Hong S, Park C. Preparation, characterization and application of low-cost pyrophyllite-alumina composite ceramic membranes for treating low-strength domestic wastewater. *J. Membr. Sci.* **2017**, *536*, 108–115. DOI:10.1016/j.memsci.2017.04.068
52. Ahmad R, Aslam M, Park E, Chang S, Kwon D, Kim J. Submerged low-cost pyrophyllite ceramic membrane filtration combined with GAC as fluidized particles for industrial wastewater treatment. *Chemosphere* **2018**, *206*, 784–792. DOI:10.1016/j.chemosphere.2018.05.045

53. Tauber E, Pepplinkhouse HJ, Middleton LW. Road surfacing aggregates from ceramic raw materials. *J. Aust. Ceram. Soc.* **1975**, *11*, 46–50.
54. Giardini AA, Kohn JA, Eckart DW, Tydings JE. The formation of coesite and kyanite from pyrophyllite at very high pressures and high temperatures. *Am. Miner.* **1961**, *46*, 976–982. Available online: https://pubs.geoscienceworld.org/msa/ammin/article-abstract/46/7-8/976/541805 (accessed on 6 March 2026).
55. Hulse CO, Graaf RB. Effect of temperature on the mechanical properties of solid pressure-trasmitting media. II. Pyrophyllite. *J. Appl. Phys.* **1965**, *36*, 1593–1596. DOI:10.1063/1.1703092
56. Tao ZC, Pu Z-X. Types and phase transitions of the Chaochiatai pyrophyllite with special reference to their influence on diamond synthesis. *Sci. Geol. Sin. New York* **1977**, *20*, 75–88. Available online: https://pascal-francis.inist.fr/vibad/index.php?action=getRecordDetail&idt=PASCALGEODEBRGM7820011919 (accessed on 6 March 2026).
57. Tingle TN. Retrieval of uncracked single crystals from high pressure in piston-cylinder apparatus. *Am. Miner.* **1988**, *73*, 1195–1197. Available online: https://pubs.geoscienceworld.org/msa/ammin/article-abstract/73/9-10/1195/105044 (accessed on 6 March 2026).
58. Qin X, Zhao J, Wang J, He M. Atomic structure, electronic and mechanical properties of pyrophyllite under pressure: A first-principles study. *Minerals* **2020**, *10*, 778. DOI:10.3390/min10090778
59. Tauber E, Pepplinkhouse HJ. Ceramic properties of pyrophyllite from Pambula, New South Wales. *J. Aust. Ceram. Soc.* **1972**, *8*, 62–64.
60. Tauber E, Pepplinkhouse HJ, Murray MJ. Stoneware bodies based on pyrophyllite. *J. Aust. Ceram. Soc.* **1973**, *9*, 47–51.
61. Tauber E, Murray MJ, Middleton LW. Earthenware tile body based on pyrophyllite and ortophosphoric acid. *J. Aust. Ceram. Soc.* **1974**, *16*, 46–49.
62. Tauber E, Pepplinkhouse HJ, Crook DN. Replacement of silica by pyrophyllite in vitreous china products. *Interceram.* **1976**, *25*, 195–198. Available online: https://pascal-francis.inist.fr/vibad/index.php?action=getRecordDetail&idt=PASCAL7760139521 (accessed on 6 March 2026).
63. Tauber E, Pepplinkhouse HJ, Crook DN. Development of a china (porcelain) body from Australian minerals. *Interceram.* **1977**, *26*, 211–214. Available online: https://pascal-francis.inist.fr/vibad/index.php?action=getRecordDetail&idt=PASCAL7860177744 (accessed on 6 March 2026).
64. Amritphale SS, Bhasin S, Chandra N. Energy efficient process for making pyrophyllite-based ceramic tiles using phosphoric acid and mineralizers. *Ceram. Int.* **2006**, *2*, 181–187. DOI:10.1016/j.ceramint.2005.02.002
65. Rieger KC. What raw materials can do to cut energy consumption? *Ceram. Eng. Sci. Prod.* **1980**, *1*, 842–847. DOI:10.1002/9780470291047.ch32
66. Mukhopadhyay TK, Ghatak S, Maiti HS. Effect of pyrophyllite on the mullitization in triaxial porcelain system. *Ceram. Int.* **2009**, *35*, 1493–1500. DOI:10.1016/j.ceramint.2008.08.002
67. Mukhopadhyay TK, Ghatak S, Maiti HS. Effect of pyrophyllite incorporation in porcelain composition on mechanical properties and microstructure. *Ceram. Int.* **2009**, *35*, 2555–2562. DOI:10.1016/j.ceramint.2009.01.003
68. Mukhopadhyay TK, Ghatak S, Maiti HS. Pyrophyllite as raw material for ceramic applications in the perspective of its pyro-chemical properties. *Ceram. Int.* **2010**, *36*, 909–916. DOI:10.1016/j.ceramint.2009.10.026
69. Reddy DKH, Lee S-M, Kim J-O. A review of emerging applications of natural sericite and its composites. *World Appl. Sci. J.* **2013**, *27*, 1514–1523. Available online: https://www.researchgate.net/profile/Seung-Mok-Lee/publication/285947929_A_review_onemerging_applications_of_naturalsericite_and_its_composites/links/57877b7e08aedc252a935915/A-review-onemerging-applications-of-naturalsericite-and-its-composites.pdf (accessed on 6 March 2026).
70. Wang X, Li J-H, Guan W-M, Fu M-J, Liu L-J. Emulsion-templated high porosity mullite-corundum ceramics with sericite induced textured structures. *Mater. Des.* **2016**, *89*, 1041–1047. DOI:10.1016/j.matdes.2015.10.085
71. González-Miranda FM, Garzón E, Reca J, Pérez-Villarejo L, Martínez-Martínez S, Sánchez-Soto PJ. Thermal behaviour of sericite clays as precursors of mullite materials. *J. Thermal Anal. Calorim.* **2018**, *132*, 967–977. DOI:10.1007/s10973-018-7046-9
72. Hubble DH, Shapland JT. New demands on pouring pit refractories. *Proc. Natl. Open Heart Basic Oxygen Steel Conf.* **1971**, *54*, 152–161.
73. Jeffries EH. Application and results using unfired andalusite-pyrophyllite refractories in pre-bake mode furnaces. *Light Met.* **1977**, *20*, 383, 387.
74. Pepplinkhouse HJ, Tauber E. The formation of mullite from kaolin-gibbsite and pyrophyllite-gibbsite mixtures. *J. Aust. Ceram. Soc.* **1977**, *13*, 1–4.

75. Kulkarni AK, Upadyaya DD, Rao SUK. Studies on development of alumina substrates. *Trans. Indian Ceram. Soc.* **1982**, *41*, 25–29. DOI:10.1080/0371750X.1982.10822566
76. Vasil'eva EE. Conditions for the formation of different crystalline forms of mullite. *Steklo Keram.* **1981**, *1*, 14–15.
77. Wright PW. Reaction of zircon refractories with molten Steel. *J. Aust. Ceram. Soc.* **1984**, *20*, 47–50.
78. Pauline M, James RJ. Zircon-pyrophyllite: an economical steel ladle refractory. *Proc. Natl. Open Heart Basic Oxygen Steel Conf.* **1979**, *62*, 246–250.
79. Castro PP. Refractarios para zonas de contacto con el vidrio. *Bol. Soc. Esp. Ceram. Vidr.* **1989**, *28*, 89–96. Available online: https://dialnet.unirioja.es/servlet/articulo?codigo=7518754 (accessed on 6 March 2026).
80. Shayakhmetov US, Shayakhmetov AU, Zakharov AV, Khamidullin AR, Gazizova AT. Refractory Composites Based on Pyrophyllite Raw Materials. *Refract. Ind. Ceram.* **2018**, *59*, 241–246. DOI:10.1007/s11148-018-0214-4
81. Lee HL, Jang BK, Lee HB. Mechanical properties of β-sialon prepared from Wando (Korean) pyrophyllite. *J. Kor. Ceram. Soc.* **1986**, *23*, 17–22.
82. Sugahara Y, Fukaishi A, Kuroda K, Kato CH. The carbothermal reduction process of 2:1 type clay minerals. *Clay Sci.* **1987**, *7*, 29–40. Available online: https://www.jstage.jst.go.jp/article/jcssjclayscience1960/7/1/7_1_29/_article/-char/ja/ (accessed on 6 March 2026).
83. Mukerji J, Bandyopadhyay S. Sialons from natural aluminosilicates. *Adv. Ceram. Mater.* **1988**, *3*, 369–373. DOI:10.1111/j.1551-2916.1988.tb00236.x
84. Fabbri B, Dondi M. Clays and other raw materials for the production of sialon ceramic powders. *Ind. Ceram.* **1991**, *11*, 75–81.
85. Yang G, Yin L, Fang X, Fang M, Liu Y, Huang Z, et al. Fabrication and liquid-solid, two-phase erosion wear behaviour of β-Sialon ceramic from pyrophyllite by carbothermal reduction and nitridation. *Ceram. Int.* **2014**, *40*, 10737–10741. DOI:10.1016/j.ceramint.2014.03.061
86. Kanbara T, Yamamoto T, Ikana H, Tagana T, Imai H. Porous chemically stable, electrically conducting composites prepared by sintering mixtures of carbon and clay. *J. Mater. Sci. Lett.* **1987**, *6*, 1195–1197. DOI:10.1007/BF01729180
87. Mitrović Rajić AI, Milićević JS, Grobović Novaković D. Development of modified pyrophyllite carbon paste for carbendazim detection. *Mater. Manuf. Process.* **2023**, *38*, 1643–1649. DOI:10.1080/10426914.2022.2136386
88. Cui X, Wang L, Dong Q, Liang W, Zhao S. Synthesis and characterization of a UV-resistant ZnO/pyrophyllite nanocomposite prepared by solid-state reaction method. *Ceram. Int.* **2022**, *48*, 34084–34091. DOI:10.1016/j.ceramint.2022.08.165
89. MacKenzie KJD, Komphanchai S, Vagana R. Formation of Inorganic Polymers (Geopolymers) from 2:1 Layer Lattice Alumino Silicates. *J. Eur. Ceram. Soc.* **2008**, *28*, 177–181. DOI:10.1016/j.jeurceramsoc.2007.06.004
90. Moya JS, Cabal B, Lopez-Esteban S, Bartolomé JF, Sanz J. Significance of the formation of pentahedral aluminum in the reactivity of calcined kaolin/metakaolin and its applications. *Ceram. Int.* **2024**, *50*, 1329–1340. DOI:10.1016/j.ceramint.2023.10.304
91. Jelić D, Todorović J, Saletović M, Šmitran A, Mentus S. Thermal stability and antimicrobial properties of pure and modified pyrophyllite (PYRO/Ag) clay. *J. Therm. Anal. Calorim.* **2023**, *148*, 1669–1678. DOI:10.1007/s10973-022-11303-w
92. Mijaković S, Stanković B, Grbović Novaković J, Filipović N, Stamenić L, Manić N, et al. Impact of mechanochemical activation on the thermal and morphological characteristics of silver-doped pyrophyllite. *Mater. Chem. Phys.* **2026**, *350*, 131933. DOI:10.1016/j.matchemphys.2025.131933
93. Heller L. The thermal transformation of pyrophyllite to mullite. *Am. Miner.* **1962**, *47*, 156–157. Available online: https://pubs.geoscienceworld.org/msa/ammin/article-abstract/47/1-2/156/541875 (accessed on 6 March 2026).
94. Nakahira M, Kato T. Thermal transformations of pyrophyllite and talc as revealed by X-ray and electron diffraction studies. In *Clays and Clay Minerals (National Conference on Clays and Clay Minerals)*; Cambridge University Press & Assessment: Cambridge, UK, 1963; pp. 21–27.
95. Frost RL, Barron PF. Solid-State Si-29 and Al-27 Nuclear Magnetic Resonance Investigation of the Dehydroxylation of Pyrophyllite. *J. Phys. Chem.* **1984**, *88*, 6206–6209. DOI:10.1021/j150669a030
96. Komarneni S, Fyfe CA, Kennedy GJ. Order-Disorder in 1:1 Type Clay Minerals by Solid-State ^{27}Al and ^{29}Si Magic Angle Spinning NMR Spectroscopy. *Clay Miner.* **1985**, *20*, 327–334. DOI:10.1180/claymin.1985.020.3.05
97. MacKenzie KJD, Brown IWH, Meinhold RH, Bowden ME. Thermal Reactions of Pyrophyllite Studied by High-Resolution Solid-State ^{27}Al and ^{29}Si Nuclear Magnetic Resonance Spectroscopy. *J. Am. Ceram. Soc.* **1985**, *68*, 266–272. DOI:10.1111/j.1151-2916.1985.tb15320.x
98. Sánchez-Soto PJ, Pérez-Rodríguez JL. Thermal analysis of pyrophyllite transformations. *Thermochim. Acta* **1989**, *138*, 267–276. DOI:10.1016/0040-6031(89)87263-6

99. Fitzgerald JJ, Dec SF, Hamza AI. Observation of Five-Coordinated Al in Pyrophyllite dehydroxylate by Solid-State ^{27}Al NMR Spectroscopy at 14 T. *Am. Miner.* **1989**, *74*, 1405–1408. Available online: https://pubs.geoscienceworld.org/msa/ammin/article-abstract/74/11-12/1405/42224 (accessed on 6 March 2026).
100. Sánchez-Soto PJ, Sobrados I, Sanz J, Pérez-Rodríguez JL. ^{29}Si and ^{27}Al Magic-Angle Nuclear Magnetic Resonance Study of the Thermal Transformations of Pyrophyllite. *J. Am. Ceram. Soc.* **1993**, *76*, 3024–3028. DOI:10.1111/j.1151-2916.1993.tb06604.x
101. Drits VA, Besson G, Muller F. An Improved Model for Structural Transformations of Heat-Treated Aluminous Dioctahedral 2:1 Layer Silicates. *Clays Clay Miner.* **1995**, *43*, 718–731. DOI:10.1346/CCMN.1995.0430608
102. Drits VA, Derkowski A, McCarty DK. New insight into the structural transformation of partially dehydroxylated pyrophyllite. *Am. Miner.* **2011**, *96*, 153–171. DOI:10.2138/am.2011.3605
103. Fitzgerald JJ, Hamza AI, Dec SF, Bronnimann CE. Solid-State ^{27}Al and ^{29}Si NMR and ^{1}H Cramps Studies of the Thermal Transformation of the 2:1 Phyllosilicate Pyrophyllite. *J. Phys. Chem.* **1996**, *100*, 17351–17360. DOI:10.1021/jp961499f
104. Sánchez-Soto PJ, Pérez-Rodríguez JL, Sobrados I, Sanz J. Influence of Grinding in Pyrophyllite-Mullite Thermal Transformation Assessed by ^{29}Si and ^{27}Al MAS NMR Spectroscopies. *Chem. Mater.* **1997**, *9*, 677–684. DOI:10.1021/cm960224+
105. Wang L, Zhang M, Redfern SAT, Zhang ZY. Dehydroxylation and Transformations of the 2:1 Phyllosilicate Pyrophyllite at Elevated Temperatures: An Infrared Spectroscopic Study. *Clays Clay Miner.* **2002**, *50*, 272–283. DOI:10.1346/000986002760832874
106. Sanz J, Madani A, Serratosa JM, Moya JS, Aza S. Aluminum-27 and Silicon-29 Magic Angle Spinning Nuclear Magnetic Resonance Study of the Kaolinite-Mullite Transformation. *J. Am. Ceram. Soc.* **1988**, *71*, C418–C421. DOI:10.1111/j.1151-2916.1988.tb07513.x
107. Molina-Montes E, Donadio D, Hernandez-Laguna A, Sainz-Diaz CI, Parrinello M. DFT Research on the Dehydroxylation Reaction of Pyrophyllite. 1. First-Principle Molecular Dynamics Simulations. *J. Phys. Chem. B* **2008**, *112*, 7051–7060. DOI:10.1021/jp711278s
108. Molina-Montes E, Donadio D, Hernandez-Laguna A, Sainz-Diaz CI. DFT Research on the Dehydroxylation Reaction of Pyrophyllite. 2. Characterization of Reactants, Intermediates, and Transition States along the Reaction Path. *J. Phys. Chem. B.* **2008**, *112*, 6373–6383. DOI:10.1021/jp8010876
109. Pérez-Rodríguez JL, Duran A, Sánchez Jiménez PE, Franquelo ML, Perejón A, Pascual-Cosp J, et al. Study of the Dehydroxylation-Rehydroxylation of Pyrophyllite. *J. Am. Ceram. Soc.* **2010**, *93*, 2392–2398. DOI:10.1111/j.1551-2916.2010.03750.x
110. Aksay IA, Pask JA. Stable and metastable equilibrium in the system SiO_2–Al_2O_3. *J. Am. Ceram. Soc.* **1975**, *58*, 507–512. DOI:10.1111/j.1151-2916.1975.tb18770.x
111. Aksay IA, Dabbs DM, Sarikaya M. Mullite for structural, electronic and optical applications. *J. Am. Ceram. Soc.* **1991**, *74*, 2343–2358. DOI:10.1111/j.1151-2916.1991.tb06768.x
112. Castelein O, Soulestin B, Bonnet J, Blanchart P. The influence of heating rate on the thermal behavior and mullite formation from a kaolin raw material. *Ceram. Int.* **2001**, *27*, 517–522. DOI:10.1016/S0272-8842(00)00110-3
113. Schneider H, Schreuer J, Hildmann B. Structure and properties of mullite—A review. *J. Eur. Ceram. Soc.* **2008**, *28*, 329–344. DOI:10.1016/j.jeurceramsoc.2007.03.017
114. Boussois K, Deniel S, Tesisier-Doyen N, Chateigner D, Dublanche-Tixier C, Blanchart P. Characterization of textured ceramics containing mullite from phyllosilicates. *Ceram. Int.* **2013**, *39*, 5327–5333. DOI:10.1016/j.ceramint.2012.12.038
115. Pérez-Rodríguez JL, Maqueda C, Justo A. Pyrophyllite determination in mineral mixtures. *Clays Clay Miner.* **1985**, *33*, 563–566. DOI:10.1346/CCMN.1985.0330614
116. Maqueda C, Pérez-Rodríguez JL, Justo A. Problems in the dissolution of silicates by acid mixtures. *Analyst* **1986**, *111*, 1107–1108. DOI:10.1039/AN9861101107
117. Maqueda C, Pérez-Rodríguez JL, Justo A. Effect of pyrophyllite on the precipitation of aluminium sulphate during the dissolution of aluminosilicates by acid mixtures. *Analyst* **1987**, *112*, 1085–1086. DOI:10.1039/AN9871201085
118. Garzón E, Sánchez-Soto PJ. An improved method for determining the external specific surface area and the plasticity index of clayey samples based on a simplified method for non-swelling fine-grained solids. *Appl. Clay Sci.* **2015**, *115*, 97–107. DOI:10.1016/j.clay.2015.07.015
119. Jena SK, Singh S, Rao DS, Dhawan N, Misra PK, Das B. Characterization and removal of iron from pyrophyllite ore for industrial applications. *Min. Metall. Explor.* **2015**, *32*, 102–110. DOI:10.1007/BF03402427
120. Harvey CC, Murray HH. Industrial clays in the 21st century: A perspective of exploration, technology and utilization. *Appl. Clay Sci.* **1997**, *11*, 285–310. DOI:10.1016/S0169-1317(96)00028-2

121. Hubbe MA, Gill RA. Fillers for Papermaking: A Review of their Properties, Usage Practices, and their Mechanistic Role. *Bioresources* **2016**, *11*, 2886–2963. DOI:10.15376/biores.11.1.Hubbe
122. Sánchez-Soto PJ, Macías M, Pérez-Rodríguez JL. Effects of Mechanical Treatment on X-ray Diffraction Line Broadening in Pyrophyllite. *J. Am. Ceram. Soc.* **1993**, *76*, 180–184. DOI:10.1111/j.1151-2916.1993.tb03704.x
123. Sánchez-Soto PJ, Jiménez de Haro MC, Pascual J, Raigón M, Pérez-Rodríguez JL. Influence of mechanical and thermal treatments on raw materials containing pyrophyllite. *Bol. Soc. Esp. Ceram. Vidr.* **2000**, *39*, 119–134. DOI:10.3989/cyv.2000.v39.i1.881
124. Gücek A, Şener S, Bilgen S, Mazmancı MA. Adsorption and kinetic studies of cationic and anionic dyes on pyrophyllite from aqueous solutions. *J. Colloid. Interf. Sci.* **2005**, *286*, 53–60. DOI:10.1016/j.jcis.2005.01.012
125. Zhang J, Yan J, Sheng J. Dry grinding effect on pyrophyllite-quartz natural mixture and its influence on the structural alternation of pyrophyllite. *Micron* **2015**, *71*, 1–6. DOI:10.1016/j.micron.2014.12.005
126. Ahmed HAM, Khairy N, Ali MA. Iron Removal from Low-Grade Pyrophyllite Ore by Microwave Irradiation and Dry Magnetic Separation. *Appl. Sci.* **2024**, *14*, 6651. DOI:10.3390/app14156651
127. Rajić MA, Gloginjić M, Mravik Ž, Milošević Govedarović S, Novaković N, Pantić T, et al. Raman spectroscopy study of structural changes in pyrophyllite ore minerals induced by mechanochemical milling. *Powder Technol.* **2024**, *448*, 120291. DOI:10.1016/j.powtec.2024.120291
128. Pask JA, Tomsia AP. Formation of mullite from sol-gel mixtures and kaolinite. *J. Am. Ceram. Soc.* **1991**, *74*, 2367–2373. DOI:10.1111/j.1151-2916.1991.tb06770.x
129. Sánchez-Soto PJ, García-Garzón V, Martínez-Martínez S, Pérez-Villarejo L, Sánchez-Garrido JA, Garzón E. Influence of features and firing temperature on the ceramic properties and phase evolution of raw kaolins. *Contr. Build. Mater.* **2025**, *466*, 140215. DOI:10.1016/j.conbuildmat.2025.140215
130. Sánchez-Soto PJ, Justo A, Pérez-Rodríguez JL, Morillo E. Structural Alteration of Pyrophyllite by Dry Grinding as Studied by IR Spectroscopy. *J. Mater. Sci. Lett.* **1994**, *13*, 915–918. DOI:10.1007/BF00273248
131. Inoue K, Okuda S. Abnormal expansion of pyrophyllite and sericite compacts during dehydroxylation. *J. Ceram. Assoc. Jpn.* **1973**, *81*, 91–96. DOI:10.2109/jcersj1950.81.931_91
132. Schomburg J. Thermal investigations of pyrophyllites. *Thermochim. Acta* **1985**, *93*, 521–524. DOI:10.1016/0040-6031(85)85131-5
133. Shamim M, Mukhopadhyay TK, Dana K. Kinetics pathway for thermal exfoliation of pyrophylite. *Appl. Clay Sci.* **2015**, *114*, 40–47. DOI:10.1016/j.clay.2015.05.006
134. Shamim M, Molla AR, Mukhopadhyay TK, Dana K. Non-Isothermal Kinetic Evaluation of Pyrophyllite Dehydroxylation. *Trans. Ind. Ceram. Soc.* **2014**, *73*, 181–186. DOI:10.1080/0371750X.2014.922434
135. Chester JH. *Refractories Production and Properties*; The Iron and Steel Institute: London, UK, 1973; pp. 262–324.
136. Perrotta A, Grubbs DK, Martin ES, Nando NR, McKinstry HA, Huarg CY. Chemical stabilization of β-Cristobalite. *J. Am. Ceram. Soc.* **1989**, *72*, 441–447. DOI:10.1111/j.1151-2916.1989.tb06150.x
137. Stevens SJ, Hand RJ, Sharp JH. Temperature dependence of the cristobalite α-β inversion. *J. Thermal Anal.* **1997**, *49*, 1409–1415. DOI:10.1007/BF01983699
138. Pascova R, Avdeev G, Gutzow I, Penkov I, Ludwig FP, Schmelzer JW. Refractory alkali-free cristobalite glass-ceramics: Activated reaction sinter-crystallization synthesis and properties. *Int. J. Appl. Glass Sci.* **2012**, *3*, 75–87. DOI:10.1111/j.2041-1294.2011.00072.x
139. Thieme K, Ortmann L, Thieme C. Microstructural insights into the stabilization of β-cristobalite. *Ceram. Int.* **2025**, *51*, 33800–33810. DOI:10.1016/j.ceramint.2025.05.114
140. Li DX, Thomson WJ. Tetragonal to orthorhombic transformation during mullite formation. *J. Mater. Res.* **1991**, *6*, 819–824. DOI:10.1557/JMR.1991.0819
141. Levin EM, Robbins CR, McMurdie HF. System SiO_2–Al_2O_3–K_2O, p. 156, Plate 407. In *Phase Diagrams for Ceramists*; The American Ceramic Society: Columbus, OH, USA, 1964.
142. Sánchez-Soto PJ, Eliche-Quesada D, Martínez-Martínez S, Garzón E, Pérez-Villarejo L, Rincón JM. The effect of vitreous phase on mullite and mullite-based ceramic composites from kaolin wastes as by-products of mining, sericite clays and kaolinite. *Mater. Let.* **2018**, *223*, 154–158. DOI:10.1016/j.matlet.2018.04.037
143. Sánchez-Soto PJ, Garzón E, Pérez-Villarejo L, Angelopoulos GN, Eliche-Quesada D. Mining Wastes of an Albite Deposit as Raw Materials for Vitrified Mullite Ceramics. *Minerals* **2021**, *11*, 232. DOI:10.3390/min11030232
144. Konopicky K. La constitution des matériaux réfractaires silico-alumineux et les facteurs donc elle dépend. *Silic. Ind.* **1962**, *27*, 7–16.
145. McGee TD. Constitution of fire-clays at high temperatures: I, II and III. *J. Am. Ceram. Soc.* **1966**, *49*, 83–94.

146. Sánchez-Soto PJ, Garzón E, Pérez-Villarejo L, Eliche-Quesada D. Sintering behaviour of a clay containing pyrophyllite, sericite and kaolinite as ceramic raw material: Looking for the optimum firing conditions. *Bol. Soc. Esp. Ceram. Vidr.* **2023**, *62*, 26–39. DOI:10.1016/j.bsecv.2021.09.001
147. Garzón E, Pérez-Villarejo L, Eliche-Quesada D, Martínez-Martínez S, Sánchez-Soto PJ. Vitrification rate and estimation of the optimum firing conditions of ceramic materials from raw clays: A review. *Ceram. Int.* **2022**, *48*, 15889–15898. DOI:10.1016/j.ceramint.2022.02.129
148. Sánchez-Soto PJ, Eliche-Quesada D, Martínez-Martínez S, Pérez-Villarejo L, Garzón E. Study of a Waste Kaolin as Raw Material for Mullite Ceramics and Mullite Refractories by Reaction Sintering. *Materials* **2022**, *15*, 583. DOI:10.3390/ma15020583